



CFD modeling of date palm (*Phoenix dactylifera*) waste fast pyrolysis in a fluidized bed-including experimental kinetics, validation, and remarks on the modeling approach

Yassir Makkawi^{*}, Baraa Mohamed

Bioenergy and Solar Conversion Research Group (BSCRG), College of Engineering, American University of Sharjah, P.O. Box 26666, Sharjah, United Arab Emirates

CFD modeling of date palm (*Phoenix dactylifera*) waste fast pyrolysis in a fluidized bed-including experimental kinetics, validation, and remarks on the modeling approach

Yassir Makkawi^{*} and Baraa Mohamed

Bioenergy and Solar Conversion Research Group (BSCRG), College of Engineering, American University of Sharjah, P.O. Box 26666, Sharjah, United Arab Emirates (UAE).

Abstract:

The current estimate of worldwide date palm waste is ~3.8 million tons annually, with only 10% recycled and the rest discarded in landfills. This improper disposal leads to environmental concerns, including methane release and groundwater contamination. This study developed and experimentally validated a computational model of date palm waste fast pyrolysis in a fluidized bed reactor. The model employed a single-step devolatilization reaction scheme in a Eulerian-Eulerian CFD framework. The reaction kinetics were experimentally derived from thermogravimetric analysis of the feedstock and pyrolysis products. The pyrolysis was simulated at three different temperatures (450, 525, and 580 °C). The impact of tar (bio-oil) thermal cracking on the pyrolysis yield was investigated using a model derived from lignocellulose biomass. At a pyrolysis temperature of 525 °C, the devolatilization efficiency was 70.1%, and the predicted

^{*} Corresponding author: Tel.: +97165152167; fax: +97165152979. E-mail address: ymakkawi@aus.edu (Yassir T. Makkawi).

product composition was 41.2% bio-oil, 37.6% char, and 21.2% non-condensable gases, which closely matched the experimental findings. The mean gas residence time over the temperature range investigated was 0.38-0.45 seconds, falling within the recommended range for fast pyrolysis. Increasing the temperature beyond approximately 500 °C decreased bio-oil yield, primarily due to the thermal cracking of tar. Remarks on the modeling approach and implementation for large-scale simulation are discussed.

Keywords: Pyrolysis, Date palm waste, Eulerian-Eulerian, CFD, Fluidized bed, Reaction kinetics.

1 Introduction

Biomass fast pyrolysis is an attractive process for converting organic matter into liquid fuel (bio-oil), gas, and biochar. It is also predicted to play an important role in future waste management by turning organic solid waste into valuable products instead of sending it to landfills [1]. Recent reports suggest that the global population of date palm trees, which ranges from 100 to 120 million, generates a substantial quantity of biomass residue (approximately 15-35 kg per tree) annually [2,3]. Fast pyrolysis involves rapidly heating the solid matter in an inert environment to produce hydrocarbon vapor and biochar. Upon fast cooling of the vapor (quenching), a high-energy content liquid (bio-oil) is formed alongside a non-condensable fraction of light gases. The process is optimized to maximize the bio-oil production by controlling the pyrolysis temperature, reducing the pyrolysis vapor residence time, and limiting the contact between the pyrolysis vapor and the biochar. These are essential conditions to prevent secondary cracking of the pyrolysis vapor into light gases [4,5].

Fluidized beds are widely viewed as one of the best types of gas-agitated multiphase reactors. It has several attractive features; simple design, good mixing of the bed material, continuous operation, and good scale-up potentials [6,7]. In the context of biomass fast pyrolysis, fluidized beds are particularly attractive due to their rapid biomass decomposition through the large surface area, uniform temperature distribution, efficient heat transfer between phases, and short gas residence time controlled by the velocity of the fluidizing medium [5]. In computational modeling, accurate prediction of the biomass particle's behavior and the evolution of products following reactions within a fluidized bed is challenging. This requires careful modeling and simulation of the flow field (particle-particle and gas-particle interactions) and reaction rates (pyrolysis kinetics) without excessive computational time and memory. If the biomass decomposition kinetics is given,

a single isolated single biomass particle undergoing thermal decomposition can be modeled by using analytical and numerical solutions decoupled from the hydrodynamic transport phenomena. For example, Li et al. [8] developed a computational model in C++ programming language to study the pyrolysis of a single biomass pellet using a one-step devolatilization reaction. With such an approach, the time and space evolution of the heat and mass transfer, decomposition rate, and yield at the single particle level was obtained with great accuracy within a very short computational time. Building on this, computational models of fluidized bed pyrolysis can be developed by incorporating the reaction kinetics in a Eulerian-Eulerian (two-fluid) [9,10] or Eulerian-Lagrangian models for multiphase flow hydrodynamics [11,12]. The flow behavior, mixing, heat transfer, and reaction kinetics within a fluidized bed reactor can be predicted using the Eulerian-Eulerian model. This model is computationally inexpensive compared to more detailed particle-based models, such as the Eulerian-Lagrangian model (discrete element method, DEM), which explicitly tracks individual particles using Newton's second law. The Eulerian-Eulerian model is also suitable for large-scale simulations of the fluidized bed and can provide valuable insights into the detailed hydrodynamics, such as the bed material hold-up and velocities, which determines, among others, the volume of the reactor for design and scale-up [13,14]. Similarly, the models can be used to predict various aspects of the fluidized bed pyrolysis operation, such as the spatial temperature distribution, rate of the vapor release, the overall product yield (bio-oil, biochar, and gas), and determine the optimal temperature for a maximum bio-oil yield [9,15]. Alongside the computational methods, laboratory-scale experimentation of fluidized bed pyrolysis can be used to aid in the design and optimization of operating conditions and provide the data required for model validation. However, due to the high-temperature operation and the challenges associated with gaseous and particulate emissions within the lab space, experimentation with fluidized bed pyrolysis is often complicated, expensive, and requires a careful, safe set-up. This is even more complex when conducting parametric analysis experiments with various operating conditions. As a result, creating reliable computational models becomes crucial for the industrial-scale design and implementation of fluidized bed pyrolysis.

In the past five years, the literature has documented seventy-five research papers dedicated to the computational modeling of fluidized bed pyrolysis (according to Scopus search with keywords: fluidized bed, CFD, pyrolysis). However, despite the significant impact of biomass feedstock

characteristics on the reactor performance and products, none of these papers have considered fast pyrolysis of date palm waste. Furthermore, only nine considered three-dimensional simulation coupling CFD with pyrolysis reactions. Hereafter a brief about some of the most recent papers and their main findings. Tokmurzin et al. [16] developed a three-dimensional model of waste plastic gasification. The model comprised gas-solid interactions, drying, pyrolysis, and heterogeneous and homogeneous gasification reactions. Expanding the chemical reaction sub-model enhanced the hydrocarbon-oxygen, hydrocarbon-steam, and tar cracking reaction sub-models. The model's accuracy was evaluated and used to simulate syngas' formation or the plastic waste's auto-thermal decomposition to C₂-C₃ hydrocarbons at low air-to-fuel equivalency ratios. In a recent study on large-scale biomass thermal conversion (1 MW), von Berg et al. [17] used a multiphase particle-in-cell (PCM) model and commercial CFD software (ANSYS Fluent) to develop a multi-scale modeling strategy for a fluidized bed biomass gasifier. The findings demonstrated that the PCM numerical approach showed better agreement with the experiment than the uniform conversion model (commonly used in the literature). However, it is complex to implement, time-consuming, and only limited to less than 80,000 reacting fuel particles and 1,200,000 bed particles. In a study using CFD with discrete element modeling (DEM), Houston et al. [18] simulated switchgrass fast pyrolysis in a bench-scale bubbling fluidized bed reactor. The biomass thermal conversion scheme was condensed into a simplified reaction scheme with secondary cracking reactions. The developed model was implemented in MFIX open-source CFD software. The steady-state yields of liquid bio-oil and non-condensable gases (NCG) at 550°C were assessed, and the effect of operational parameters was evaluated. Interestingly, the results from the simplified reaction model were identical to those obtained from a comprehensive pyrolysis reaction model, which considered the complete secondary reaction scheme. Jalalifar et al. [19] conducted a computational investigation on the parameters influencing the yields of a fast pyrolysis process in a lab-scale bubbling fluidized bed reactor. The biomass decomposition was simplified into ten reaction mechanisms. To avoid excessive computational time, the complex transport phenomena involved were modeled in two-dimensional based on Eulerian-Eulerian method coupled with reaction rates. The findings revealed that the optimal temperature range for bio-oil production was between 500 and 525 °C. Furthermore, it was demonstrated that higher nitrogen velocities lead to reduced residence time, which decreases the probability of secondary cracking of the pyrolysis vapors into non-condensable gases. Consequently, this results in an increased bio-oil yield. Hameed et al. [20]

reported a two-dimensional CFD model study of fluidized bed biomass pyrolysis using four parallel reactions with distributed activation energy (DAE). The DAE was implemented to better represent the pyrolysis reactions with different activation energies. The results indicated a significant difference between the DAE approach and the standard model of single activation energy predictions, especially in terms of the gas and biochar yield. However, despite implementing a computationally extensive and complex reaction model, there was no strong evidence of better agreement of the DAE predictions with the experimental data. Cai et al. [21] used a two-dimensional Eulerian-Eulerian model to study the effect of flow hydrodynamics on the performance of a bubbling fluidized bed pyrolysis reactor. The hydrodynamics variations were introduced by changing the positions of the fluidizing nitrogen and biomass inlets. The findings revealed that changing the biomass inlet from a single to double nozzles spraying in opposite directions led to a more uniform spatial particle distribution and temperature and increased tar yield. Moreover, a significant local circulation formed in the dense phase zone when a single nitrogen nozzle was used. However, the impact of such recalculation behavior on the gas residence time was not discussed. Another two-dimensional fluidized bed Eulerian-Eulerian simulation of biomass pyrolysis has been reported by Thoharudin et al. [22]. The drying stage was omitted, and the biomass (palm kernel shell) was assumed to directly decompose into active species of cellulose, hemicellulose, and lignin (multi-component). Each component was assumed to follow different pyrolysis kinetics to produce tar, biochar, and non-condensable gas. The findings revealed that elevating the temperature led to higher conversion efficiency and increased yields of non-condensable gas products, while higher superficial velocities of nitrogen promoted shorter gas residence times, leading to increased tar yield. Although these findings align with the experimental observations, there is still a requirement to enhance the comprehension and quantifications of how temperature influences the fluidized bed hydrodynamics and the rate of pyrolysis and secondary reactions. Ding et al. [23] used the CFD approach with the same method of a multi-component one-step pyrolysis model and the same palm kernel shell kinetics used by Thoharudin et al. [22] to simulate the pyrolysis of plastic waste in a fluidized bed reactor. The study investigated the spatial variation of temperature, product distribution, and flow regime at different pyrolysis temperatures, superficial gas velocity, and initial bed height. The findings showed that with increasing the pyrolytic temperature, the production of tar tends to decrease, while the production of gas gradually increases, and the production of char steadily decreases. These are classic features

of biomass fast pyrolysis; however, the predicted yields differed from the experimental results. The authors attributed this to certain experiment losses, which are not considered in the model, such as incomplete condensation and pipe loss. Another factor that may have contributed to such discrepancy is of using a generalized pyrolysis reaction model that does not accurately represent the feedstock used.

This paper introduces a new three-dimensional (3D) computational fluid dynamics (CFD) model to simulate the pyrolysis of date palm waste in a bubbling fluidized bed. The model utilizes a Eulerian-Eulerian approach and is implemented within ANSYS Fluent CFD simulation code (Ver 2021) [24]. The main objective is to present an experimentally validated CFD approach capable of capturing hydrodynamics and pyrolysis details of date palm waste while maintaining reasonable computational efficiency. The model incorporates a reaction framework, including a one-step (global) pyrolysis reaction and tar thermal cracking (secondary volatiles decomposition). Thermogravimetric analysis (TGA) and CHNO analysis of the biomass feedstock and pyrolysis products were employed to determine the reaction kinetics and stoichiometric coefficients. The model's validity was confirmed by comparing it to experimental data obtained in a lab-scale fluidized-bed reactor, as reported by Makkawi et al. [2]. In the conclusion section, this paper critically evaluates the proposed model, making it a valuable tool for future development and investigations of biomass pyrolysis in fluidized bed reactors.

2 Materials and Methodology

2.1 Reactor operating conditions and experimental validation

The geometry and dimensions of the fluidized bed used in the simulation were exactly matching that of the experimental reactor described in Makkawi et al. [2] (see Fig 1). The simulation domain was produced using Ansys 3D design software. The fluidizing gas (nitrogen) was introduced hot through a perforated plate from the bottom of the reactor at a velocity of 0.485 m/s. Additional nitrogen, at the flow rate of $\sim 1.0 \text{ kg h}^{-1}$ was introduced with the biomass to create a positive pressure at the feeding point. At the start of the simulation, the reactor bed was initially packed with sand of the size 0.6 mm at a static bed height of 9.5 cm and at an initial temperature similar to the fluidizing nitrogen. The upper section of the reactor wall (16.0 cm) was set at full insulation (no heat transfer) while the lower part wall (26.0 cm) was set at fixed wall temperature. Date palm

waste (biomass feedstock) particles of 0.5 mm equivalent diameter were fed to the reactor at a continuous rate of 0.3 kg h⁻¹. Summary of the reactor operating condition, as applied in the simulation, and that of the experimental validation, as reported in Makkawi et al. [2], are given in Table 1. Further details on the model validation method is given in Section 2.4.

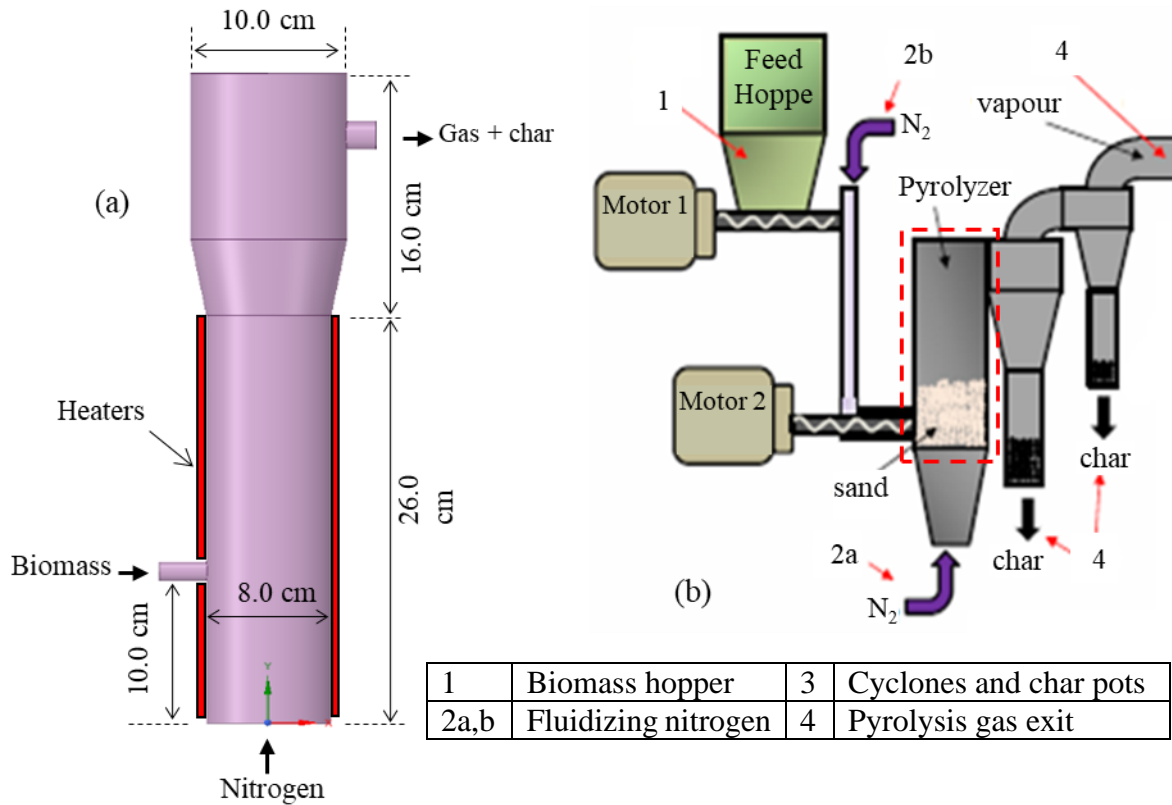


Fig. 1. (a) Geometry and dimensions of the fluidized bed reactor used in the simulation (b) Schematic of the experimental pyrolysis system used in Makkawi et al. [2] (the red dotted box indicates the simulation domain).

Table 1. Summary of the operating conditions used in the simulation and the experimental conditions of Makkawi et al. [2], as used in the model validation.

Parameter	Simulation condition	Experiment condition [2]
<i>Inert bed material (sand)</i>		
Particle diameter (mm)	0.63	0.6–0.71 (mean 0.63)
Particle bulk density (kg m ⁻³)	2600	2600
Initial temperature (°C)	500, 550, and 600	550
Static bed height (cm)	9.5	9.5
<i>Fluidizing gas (nitrogen)</i>		
Inlet temperature	500, 550, and 600	600
Superficial velocity (m s ⁻¹)	0.485	0.485
Mass flow at biomass inlet (kg h ⁻¹)*	1.0	1.0
<i>Biomass (date palm waste)</i>		
Particle size (mm)	0.55 mm	0.5–1.0 (mean 0.55)
Particle bulk density (kg m ⁻³)	536	536
Inlet temperature (°C)	25	25
Feeding rate (kg h ⁻¹)	0.3	0.3
<i>Reactor</i>		
Operation mode	Continuous fluidization	Continuous fluidization
Lower wall temperature (°C)	500, 550, and 600	550 (electric heating)
Higher wall temperature (°C)	Zero heat flux (insulated)	Insulated
Pyrolysis temperature (°C)**	480, 525, 580	525

* At 25°C.

** At the middle of the fluidized bed (6.0 cm above the distributor).

2.2 Chemical composition of the date palm waste

The main chemical characteristics of the date palm waste biomass used in the simulation are presented in Table 2. This data provided essential input parameters to define the biomass characteristics at the feed to the fluidized bed.

Table 2. Proximate (wet-basis) and ultimate analysis of the feedstock (date palm waste mixture) [2].

<i>Proximate analysis (mass %)</i>	
Moisture	10.61
Ash	10.06
Volatile	64.70
Fixed Carbon ¹	14.63
<i>Ultimate analysis (mass %)</i>	
C	42.50
H	5.78
N	0.88
S	0.19
O ²	50.65

¹ By difference from 100%.

² By difference from 100%, ash included.

2.3 Model description and solution procedure

2.3.1 Hydrodynamic model

A Eulerian-Eulerian Multi-Fluid Model (MFM) was used to simulate the fluidized bed hydrodynamics. The model employed conservation laws of mass, momentum, energy, and species, including constitutive relations derived from the Kinetic Theory of Granular Flow (KTGF). The multi-fluid flow consisted of a primary gas phase and two secondary solid phases (granular), namely biomass and sand. The continuity equations for the gas and solid phases, respectively, are given by:

$$\frac{\partial}{\partial t}(\alpha_g \rho_g) + \nabla \cdot (\alpha_g \rho_g \vec{v}_g) = S_q \quad (1)$$

$$\frac{\partial}{\partial t}(\alpha_{s_i} \rho_{s_i}) + \nabla \cdot (\alpha_{s_i} \rho_{s_i} \vec{v}_{s_i}) = S_{q_i} \quad (2)$$

where α is the volume fraction, \vec{v} is the velocity vector, ρ is density, S_q is a source term due to external influences (i.e., mass transfer or chemical reactions), and the subscript $i= 1$ or 2 refers to solid material in the fluidized bed (sand or biomass).

The rate of momentum equations for the gas and solid phases, respectively, are given by:

$$\begin{aligned} \frac{\partial}{\partial t}(\alpha_g \rho_g \vec{v}_g) + \nabla \cdot (\alpha_g \rho_g \vec{v}_g \vec{v}_g) \\ = -\alpha_g \nabla P_g + \nabla \cdot \bar{\tau}_g + \alpha_q \rho_q \vec{g} + \sum_{j=1}^2 \left[(\beta_{s_j} (\vec{v}_g - \vec{v}_{s_j}) + \vec{F}_{gs_j}) \right] \end{aligned} \quad (3)$$

$$\begin{aligned} \frac{\partial}{\partial t}(\alpha_{s_i} \rho_{s_i} \vec{v}_{s_i}) + \nabla \cdot (\alpha_{s_i} \rho_{s_i} \vec{v}_{s_i} \vec{v}_{s_i}) \\ = -\alpha_{s_i} \nabla P_{s_i} + \nabla \cdot \bar{\tau}_{s_i} + \alpha_{s_i} \rho_{s_i} \vec{g} \\ + \sum_{j=1}^2 \left[\beta_{gs_j} (\vec{v}_g - \vec{v}_{s_j}) + K_{s_i s_j} (\vec{v}_{s_i} - \vec{v}_{s_j}) + \vec{F}_{gs_i} \right] \end{aligned} \quad (4)$$

where the terms on the left sides of Eqs 3 and 4 represent the solid momentum increase and transfer, respectively, while the terms on the right sides represent the contribution of pressure (P) force, stress tensor ($\bar{\tau}$), acceleration due to gravity \vec{g} , solid–gas drag with coefficient β , solid–solid drag with coefficient K ($j = 1$ or $2, i \neq j$), momentum transfer (due to evaporation and interphase transfer due to the pyrolysis reaction). The subscript $i = 1$ or 2 refers to solid bed material in the fluidized bed (sand or biomass). Note that for the inert solid (sand), the mass transfer \vec{F}_{gs} is equal to zero.

The granular temperature (Θ), an important parameter used to relate the solid stress to the velocity fluctuations and energy loss during collisions is given by the following kinetic energy equation:

$$\begin{aligned} \frac{3}{2} \left[\frac{\partial}{\partial t} (\rho_{s_i} \alpha_{s_i} \Theta_{s_i}) + \nabla \cdot (\rho_{s_i} \alpha_{s_i} \vec{v}_{s_i} \Theta_{s_i}) \right] \\ = [-P_{s_i} \bar{I} + \bar{\tau}_{s_i}] : \nabla \vec{v}_{s_i} + \nabla \cdot (k_{\Theta_{s_i}} \nabla \Theta_{s_i}) - \gamma_{\Theta_{s_i}} + \varphi_{l_{s_i}} \end{aligned} \quad (5)$$

where the two terms on the left side of Eq. 5 represent the kinetic energy increase and transfer, respectively. In the right side, the first term represents the generation of energy by the solid stress, the second term represents the diffusion of energy with diffusion coefficient k_{Θ_s} , the third term represents the energy dissipation by collisions and the last term represents the energy exchange

between the solid phase i and the fluid. The summary of the constitutive equation used in the above-described hydrodynamic formulations are given in the Appendix Table A1.

2.3.2 Heat transfer model

The heat balance equation for the gas and solid phases, respectively, are given by:

$$\begin{aligned} \frac{\partial(\alpha_g \rho_g h_g)}{\partial t} + \nabla(\alpha_g \rho_g \vec{v}_g h_g) \\ = \alpha_g \frac{\partial P}{\partial t} + \bar{\tau}_g \cdot \nabla \vec{v}_g - \vec{q}_g + S_g + \sum_{i=1}^2 Q_{gs_i} + (\dot{m}_{s_i g} h_{s_i g} - \dot{m}_{gs_i} h_{gs_i}) \end{aligned} \quad (6)$$

$$\begin{aligned} \frac{\partial(\alpha_{s_i} \rho_{s_i} h_{s_i})}{\partial t} + \nabla(\alpha_{s_i} \rho_{s_i} \vec{u}_i h_{s_i}) \\ = \alpha_{s_i} \frac{\partial P_{s_i}}{\partial t} + \bar{\tau}_{s_i} \cdot \nabla \vec{u}_{s_i} - \vec{q}_{s_i} - S_g + Q_{s_i g} + (\dot{m}_{gs_i} h_{gs_i} - \dot{m}_{s_i g} h_{s_i g}) \end{aligned} \quad (7)$$

where h_g is the specific enthalpy of the gas phase, \vec{q} is the heat flux, S is a source term that includes the enthalpy due to the chemical reaction, Q is the intensity of the heat exchange between the gas and solid phases. The last term on the right-hand side of Eqs. 6 and 7 represent the interphase enthalpy exchange due to evaporation. The subscript $i=1$ or 2 refers to solid bed material in the fluidized bed (sand or biomass). Note that for the inert solid (sand), the mass transfer due to evaporation is zero. The heat exchange between the gas and solid is determined based on the following transfer coefficient:

$$Q_{gs_i} = \frac{6k_s \alpha_s \alpha_g Nu_s}{d_s^2} \quad (8)$$

where d_s is the biomass particle diameter, k_s is the thermal conductivity coefficient, and Nu_s is Nusselt number defined by Gunn's correlation as follows:

$$Nu_s = (7 - 10\alpha_g + 5\alpha_g^2) (1 + 0.7Re_s^{0.2}Pr^{1/3}) + (1.33 - 2.4\alpha_g + 1.2\alpha_g^2)Re_s^{0.7}Pr^{1/3} \quad (9)$$

where Re_s is the particle Reynolds number and Pr is the prandtl number.

2.3.3 Pyrolysis reactions and rate models

The biomass pyrolysis pathway adopted in this study is described schematically in Fig. 2a,b. Several assumptions have been made in developing this pathway and the subsequent reaction models. The biomass pyrolysis is assumed to commence by drying followed by thermal

decomposition to produce a solid phase residue (referred to as biochar in Fig. 1). The thermal decomposition produces a pyrolysis vapor consisting of non-condensable light gases (CO, CO₂, CH₄, H₂) and condensable heavier hydrocarbon components (referred to as tar₁) and H₂O. In the subsequent sections, the condensable fraction of tar₁ will be referred to as bio-oil.

Following various reported studies [15,25,26], it is assumed that the primary tar₁ may undergo thermal cracking (depending on the temperature and residence time) to produce more light gases and a non-condensable secondary tar (referred to as tar₂ in Fig. 2b). The secondary tar₂ is assumed to represent the compounds that are difficult to condense or eliminate (high-temperature tar containing significant quantity of poly-aromatic compounds).

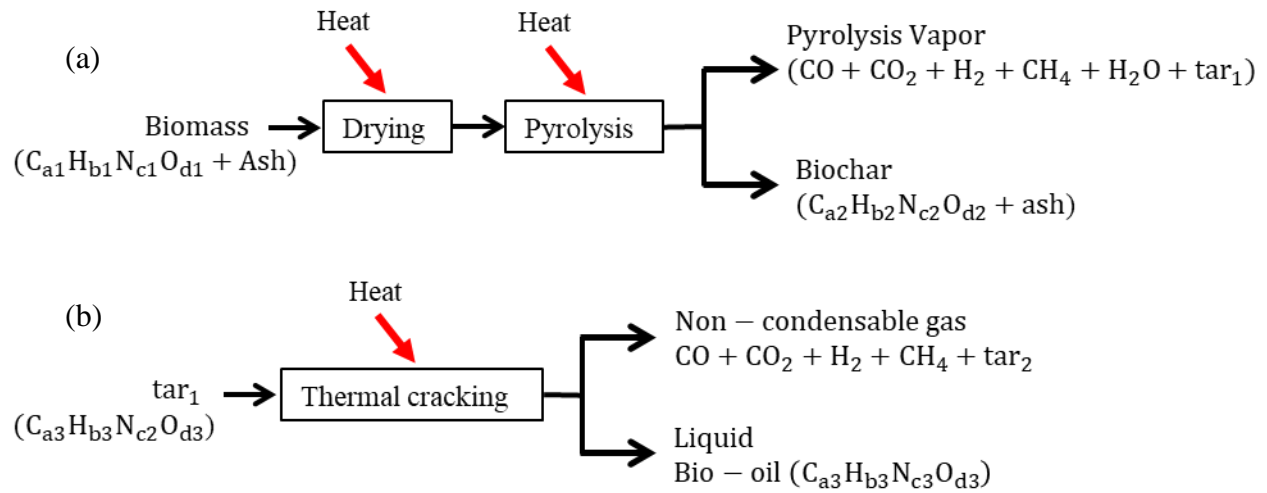


Fig. 2. Biomass thermal decomposition reaction pathway used in the simulation model (a) drying and pyrolysis (b) thermal cracking (secondary reaction).

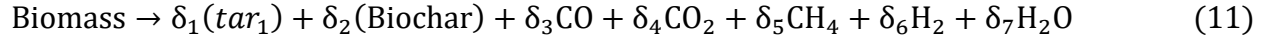
The biomass drying is implemented by an evaporation-condensation (mass transfer) model as given by the following equation [15,27]:

$$\dot{m}_{sg} = k_c \times \alpha_m \rho_m \frac{(T_{vap} - T_{sat})}{T_{sat}} \quad (10)$$

where \dot{m}_{sg} is the mass transfer rate of water from the biomass to the gas phase, k_c is the mass transfer coefficient, α_m and ρ_m represent the volume fraction and density of the water in the

biomass, T_{vap} and T_{sat} are the pyrolysis vapor phase temperature and the saturation temperature (taken as 100 °C), respectively.

The biomass devolatilization is assumed to follow a single-step reaction mechanism (global reaction) as follows:



In developing the devolatilization reaction kinetics it is first assumed that the chemical formula of the biomass and the pyrolysis products (tar₁ or bio-oil and biochar) can be well represented by their elemental composition. Accordingly, the chemical formula of the reactive biomass, primary tar₁ (bio-oil) and biochar were determined from the experimental study of Makkawi et al. [2] to be $\text{CH}_{1.632}\text{O}_{0.897}$, $\text{CH}_{0.678}\text{O}_{0.831}$ and $\text{CH}_{1.776}\text{O}_{0.633}$, respectively. The values of the stoichiometric coefficients $\delta_1 - \delta_7$, shown in Table 3, were obtained by setting three equations based on atomic balance of the elements C, H, O in Eq. 11, in addition to defining three mass balance relationships based on the non-condensable gas analysis data (see Table 2) and an overall mass balance of Eq. 11. The detailed equations used in calculating the coefficients are given in the Supplementary Material Table A2.

Table 3. Stoichiometric coefficients of the global devolatilization reaction (Eq. 11)

δ_1 (tar ₁)	δ_2 (biochar)	δ_3 (CO)	δ_4 (CO ₂)	δ_5 (CH ₄)	δ_6 (H ₂)	δ_7 (H ₂ O)
0.453	0.401	0.066	0.0841	0.023	0.00067	0.166

The devolatilization reaction was assumed to follow a simple rate model, as described below,

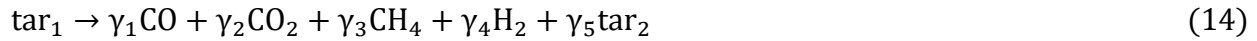
$$-r_{\text{dev}} = k_1 [C_{\text{vol}}]^{n1} \quad (12)$$

where C_{vol} is the concentration of volatile in the biomass phase, $n1$ is the reaction rate order, and k is the temperature-dependent rate constant defined in accordance with the Arrhenius equation as follows,

$$k_1 = A_1 \exp\left(\frac{-E_1}{RT}\right) \quad (13)$$

where A_1 is the frequency factor and E_1 is the activation energy. The value of $E_1 = 72.7 \times 10^3 \text{ J mol}^{-1}$ was determined by model-free approach of Kissinger [28], which involve using of experimental data of thermogravimetric analysis (TGA) at three different heating rates (5, 10, 15 $^\circ\text{C min}^{-1}$). The determined activation energy is within the range reported for date palm biomass (49.8×10^3 – $89.1 \times 10^3 \text{ J mol}^{-1}$) [3]. The values of $A_1 = 4.39 \times 10^7$ and $n = 3.1$ were determined by non-linear regression (free-model fitting) of the TGA data.

As previously mentioned, the pyrolysis vapor becomes more susceptible to thermal cracking as the temperature and gas residence time increase. The thermal cracking may also be enhanced by the catalytic effect of the metals in the biochar ash. There is no clear-cut boundary of operating temperature or gas residence time to trigger the thermal cracking, however, there is a general believe that it occurs at a temperature beyond $\sim 500 \text{ }^\circ\text{C}$ and the gas residence time beyond ~ 1 second. The thermal cracking of the primary tar₁ is represented in the model by the following reaction [15, 29]:



The value of the coefficients γ_1 – γ_5 have been taken from the reported literature as shown in Table 4. Reaction 14 is assumed to follow a first order reaction as follows [29, 30]:

$$-r_{\text{thermal}} = k_2 [C_{\text{tar}_1}] \quad (15)$$

where C_{tar_1} is the concentration of primary tar₁ in the pyrolysis vapor, and k_2 is the temperature dependent rate constant given by Arrhenius equation as follows,

$$k_2 = A_2 \exp\left(\frac{-E_2}{RT}\right) \quad (16)$$

where the values of the frequency factor (A_2) and activation energy (E_2) are taken to be $1.55 \times 10^5 \text{ s}^{-1}$ and $87.6 \times 10^3 \text{ J mol}^{-1}$, respectively [30].

Table 4. Stoichiometric coefficients of the primary tar (tar₁) thermal cracking reaction (Eq. 14) [30].

γ_1 (CO)	γ_2 (CO ₂)	γ_3 (CH ₄)	γ_4 (H ₂)	γ_5 (tar ₂)
0.4	0.1	0.1	0.2	0.2

2.3.4 Model simulation procedure

The computational domain and the boundary conditions used in the simulation of the fluidized bed reactor are shown in Fig. 3. The domain was divided into three-dimensional unstructured hexahedrons elements (grid/meshes) using ANSYS workbench software. This resulted in a total of 78470 cells, which corresponds to 15068 nodes. Finer mesh was used near the wall and interface regions to ensure capturing the steep variations of the flow field and heat flux. The solution was initially set to a time step of 0.0001 seconds and then increased to a time step of 0.001 seconds after 5 seconds of simulation time to avoid numerical instability at the start of simulation (stiffness). The number of iterations per step was set to a maximum of 50,000. The momentum equations were discretized using a first-order upwind method. This approach sets the density at the cell face to match the value at the upstream cell center. For most flow types, this discretization technique yields favorable outcomes and ensures stability in the discretization of the pressure-correction equation [24]. Applying this simulation procedure in a high-performance computing workstation equipped with a 12-Core parallel processor and 32 GB of RAM, it took approximately 5 days to complete around 25-second operation, which was sufficient for reaching steady state.

In the boundary conditions, the wall of the reactor was treated as a stationary solid with no-slip conditions (zero velocity) for the gas phase and a shear stress with 0.5 specular coefficient for the solid phases. The lower wall was assumed to be of a constant temperature while the top part was set at zero heat flux (insulated). Initially, the fluidized bed was packed with hot sand up to the height of 9.5 cm above the gas distributor. The solid volume fraction at static bed condition was set at 0.61, and the maximum packing limit was 0.63. The date palm feedstock was treated as a mixture consisting of volatiles, moisture, fixed carbon, and ash. The initial concentrations of these were obtained from the approximate analysis (see Table 2). The pyrolysis vapor is treated as a mixture consisting of CO, CO₂, CH₄, H₂, H₂O, tar₁ (bio-oil) and tar₂ (high-temperature tar). The biochar is assumed to constitute the moisture, volatile, ash and fixed carbon, remaining after the biomass thermal degradation.

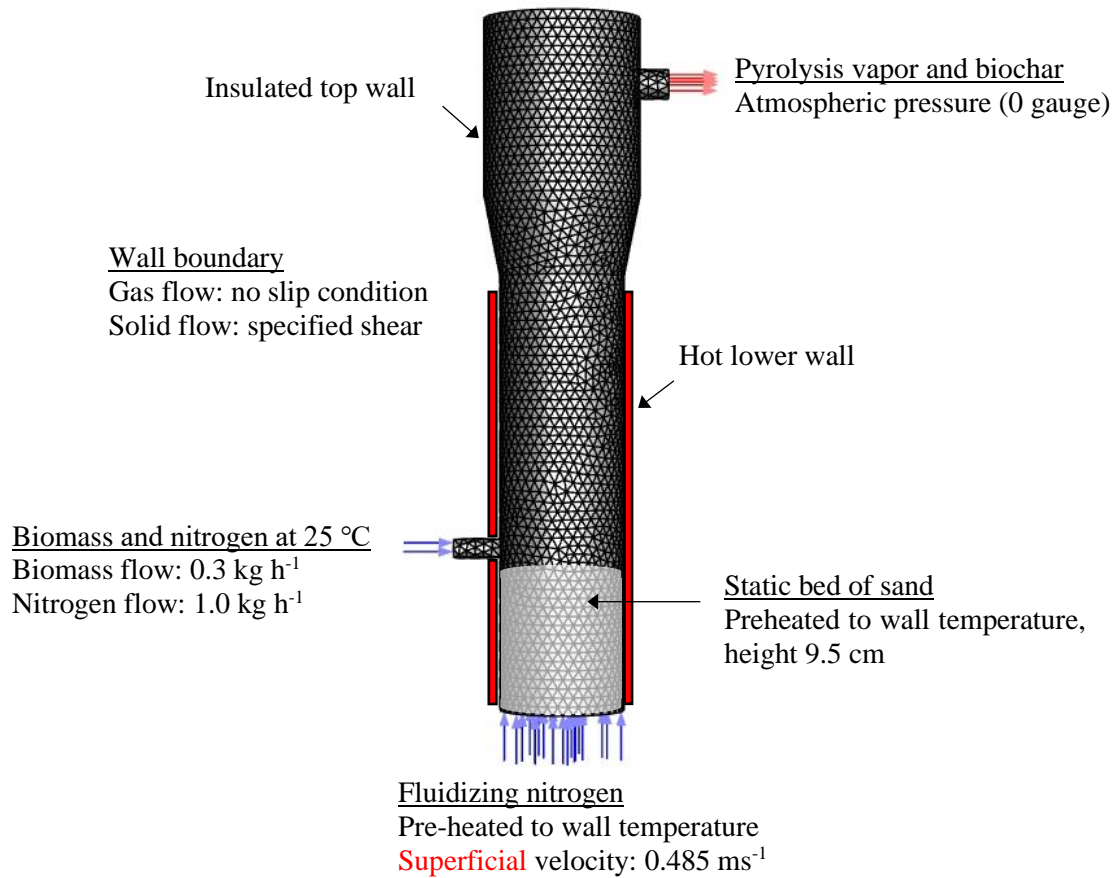


Fig. 3. Physical model of the fluidized bed showing the boundary conditions, meshing and basic operating conditions at the boundaries.

2.4 Data extraction and analysis

2.4.1 Pyrolysis yield

The distribution of the overall pyrolysis products (liquid, gas and biochar) was obtained by extracting the predicted mass flow of each of the pyrolysis product components and taking the average of the last 5 seconds data, after reaching steady state. The total gas mass flow was then given by summation of the flow rate of gas components (CO, CO₂, CH₄, H₂, and tar₂). The total pyrolysis liquid was given by the summation of the condensable fractions of the pyrolysis vapor, which includes tar₁ (bio-oil) and H₂O. The percentage biochar yield was obtained by subtraction

from 100%. Accordingly, the predicted products (liquid, biochar and non-condensable gas) distribution was given by the following equation:

$$\text{yield (\%)} = \frac{\text{mass flow rate of product at exit}}{\text{mass flow rate of biomass feed}} \times 100 \quad (17)$$

The pyrolysis yield was validated by comparison with the experimental mass balance at the pyrolysis temperature of 525 °C as reported in Makkawi et al. [2].

The water content in the pyrolysis liquid was estimated by taking the time averaged of the steady state mass flow rate of H₂O at the exit of the reactor. This given by the following equation:

$$\text{Water content in pyrolysis liquid (\%)} = \frac{\text{mass flow H}_2\text{O at exit}}{\text{mass flow rate of H}_2\text{O+tar}_1} \times 100 \quad (18)$$

The biomass devolatilization efficiency was obtained by the following equations:

$$\text{Devolatilization efficiency (\%)} = 1 - \frac{\text{mass volatiles in biochar}}{\text{mass of volatiles in the feed biomass}} \quad (19)$$

The predicted water content was validated by comparing with the experiment analysis of a single phase bio-oil using Karl Fisher titration, while the predicted devolatilization efficiency was validated by comparing it with the thermogravimetric analysis (TGA) analysis of date palm waste biochar produced at 525 °C. The details on the bio-oil and biochar collection and analysis methods are described in experimental study by Makkawi et al. [2].

2.4.2 Biochar composition and gas heating value

The predicted biochar composition was obtained by recording the mass flow rate of each of the biochar species at the exit of the reactor. The percentage composition was then calculated after taking the time-averaged data during the steady state operation and dividing by the total flow.

The high heating value (HHV) of the non-condensable gas was estimated by using the predicted gas composition (α_i) and its corresponding calorific value (CV_i) as follows [31,32]:

$$\text{HHV} = \sum_{i=1}^n (\alpha_i \times CV_i) \quad (20)$$

2.4.3 Fluidized bed temperature and gas residence time

The predicted fluidized bed temperature was obtained by recording the mixture temperature at a point in the middle of the fluidized bed. This was compared with the experimental measurement using a thermocouple inserted inside the fluidized bed, as reported in Makkawi et al. [2]. The steady state temperature at this point was then assumed to represent the pyrolysis temperature.

The distribution of the gas residence time was predicted by injecting 200 tracers (massless particles) introduced at the biomass feeding. The tracers were then tracked, and a numerical procedure was used to monitor their exit concentration as a function of time. The tracking method was implemented in ANSYS-Fluent platform to monitor the velocity field of the gas phase. The mean gas residence time, \bar{t} , was then given by the follow equation [33]:

$$\bar{t} = \frac{\int_0^{\infty} tE(t)dt}{\int_0^{\infty} E(t)dt} \quad (21)$$

where $E(t)$ is the gas residence time distribution function.

3 Results and discussion

The developed computational model provided quantitative predictions of the pyrolysis product (pyrolysis liquid, biochar and gas), in addition to detailed hydrodynamics and thermochemical features of the reactor. The first part of the results describes experimental validation of a base case scenario at the pyrolysis temperature of 525 °C. The second part shows the impact of pyrolysis temperature on the hydrodynamic features, temperature distribution, gas residence and the model sensitivity to thermal cracking. The last part presents remarks on the model approach and its limitations.

3.1 Model validation

3.1.1 Pyrolysis products distribution

The predicted pyrolysis products distribution and non-condensable gas composition in comparison to the experimental data at the pyrolysis temperature of 525 °C (base case) are shown in Fig. 4. The results indicate good capabilities of the model in predicting the overall pyrolysis products distribution (Fig. 4a) (see the evolution of some of the pyrolysis vapor components in the Supplementary material Fig. A1). The predicted liquid yield (41.2 mass %) is 6% overestimated

compared to the experimental value. The predicted biochar yield, which is 37.6%, is only 1% underestimated. The water content in the liquid, which is assumed to arise from the biomass drying and devolatilization reaction (Eqs. 10 and 11, respectively), is predicted to represent 36.7% of the total liquid, which is in excellent agreement with the experimental value of 36.3%.

In Figure 4b, the comparison between the predicted and measured composition of the non-condensable gas shows overall satisfactory results. However, there are some discrepancies concerning the concentrations of CO₂ and the heavy non-condensable gases C₁-C₄ (collectively representing the gas compounds C₂H₄, C₂H₆, C₃H₈, and C₄H₁₀). The energy content, calculated based on the mass fraction of the gas components as given in Eq. 19, yields a Higher Heating Value (HHV) of 17.2 MJ kg⁻¹, whereas the experimental value is 12.1 MJ kg⁻¹. The contribution of C₁-C₄ to the gas calorific value is considerable; however, these components are not the main source of the discrepancy because neglecting them results in an 18% overprediction. On the other hand, neglecting the contribution of H₂ results in a 37% overprediction, while neglecting the contribution of CO results in a 50% overprediction.

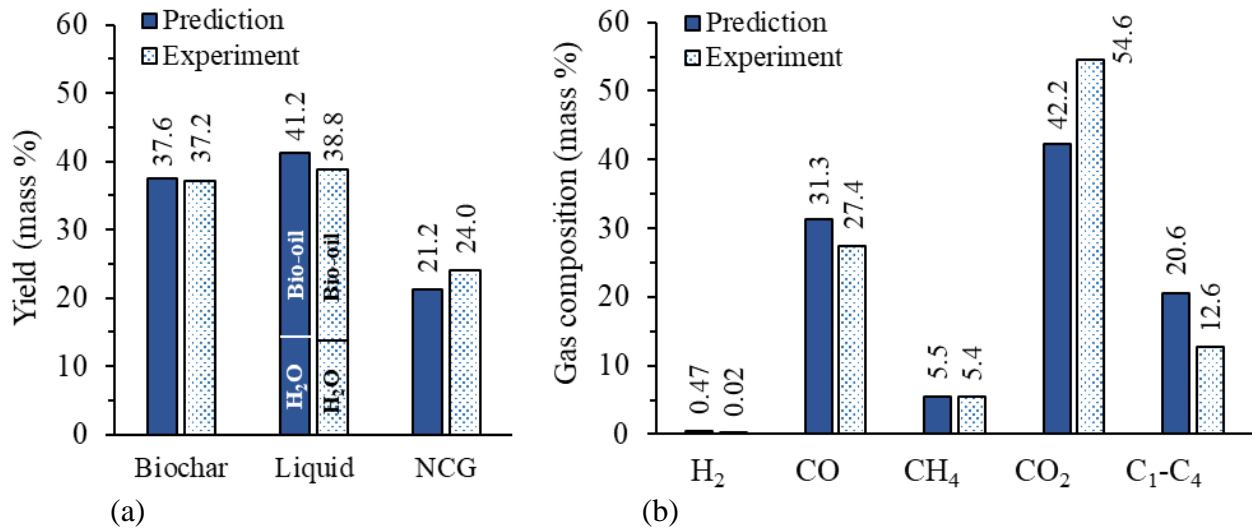


Fig. 4. Comparison of the predicted and experimental data [2] at the pyrolysis temperature of 525 °C (a) overall product yield (b) non-condensable gas composition.

3.1.2 Biochar composition and devolatilization efficiency

The predicted biochar composition in comparison with the experimental measurement is shown in Fig. 5. The result indicates reasonable capabilities of the model in predicting the biochar composition. There is relatively high discrepancy in terms of the ash concentrations, and this is mainly attributed to over-prediction of the biochar fixed carbon.

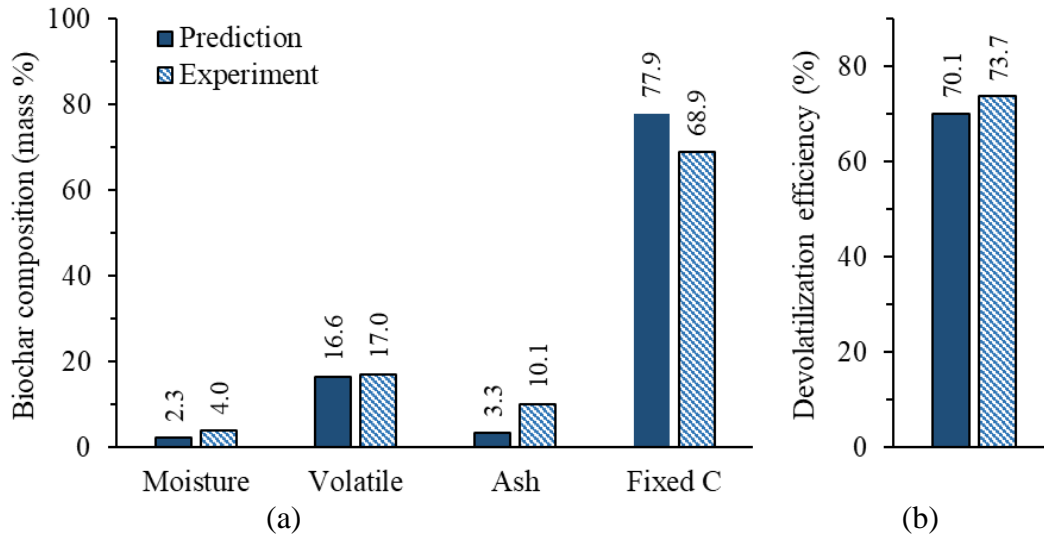


Fig. 5. Comparison of the predicted and experimental data [2] at the pyrolysis condition of 525 °C (a) biochar composition (b) devolatilization efficiency.

3.1.3 Fluidized bed temperature and gas flow

The predicted and measured fluidized bed temperature as function of the operation time is shown in Fig. 6. This figure also includes the variation of the pyrolysis vapor flow rate at the exit of the reactor. In the experimental study of Makkawi et al. [2] the temperature was obtained by collecting data every one minute using a thermocouple inserted inside the fluidized bed, while the predicted temperature was obtained by collecting data every one second during the simulation time at the same position. At steady state, the result demonstrates a good match between the experiment and prediction bed temperature. The time to reach steady state is different; in the experiment was around 25 minutes compared to around 35 seconds in the simulation. This is due to the difference between the experiment heating and the simulation procedure, where's in the former case the time to heat the bed material was counted and the biomass was only fed to the reactor after the bed

reaches the desired pyrolysis temperature, while in the model solution procedure, the initial bed temperature was set at the desired pyrolysis temperature from the beginning and the biomass was introduced right at the start, i.e., bed heating time omitted.

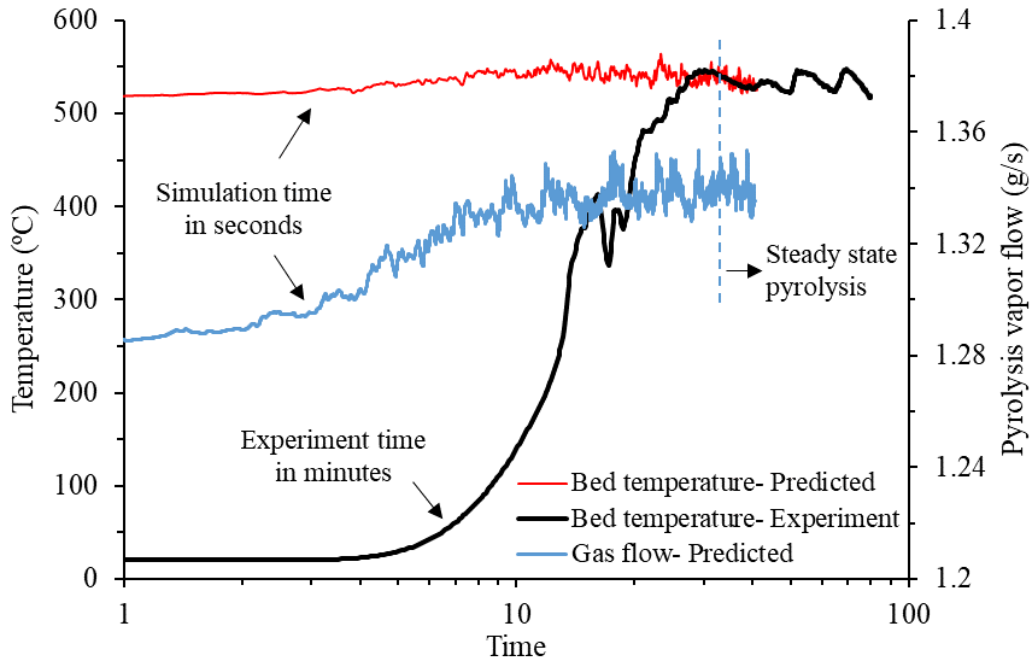


Fig. 6. Comparison of the predicted and experimental [2] fluidized bed temperature and the corresponding prediction of the pyrolysis vapor flow rate at the pyrolysis temperature of 525.

3.2 Parametric and sensitivity analysis

3.2.1 Effect of thermal cracking on pyrolysis yield

The effect of the pyrolysis temperature on the overall yield (liquid, biochar, and non-condensable gas) is illustrated in Fig. 7 in comparison to the experimental measurement at 525 °C. The results produced with a model incorporating tar thermal cracking (Eq. 14), shown in Fig. 7a, indicate that the biochar yields decrease, and the non-condensable gas (NCG) increases at increasing the pyrolysis temperature, and this comes at the expense of decreasing the bio-oil yield. This trend is a characteristic feature of fast pyrolysis commonly observed in experimental studies [e.g., 5, 34]. The prediction is also in good agreement with the experimental yield at the pyrolysis temperature of 525 °C. On the contrary, the predicted pyrolysis yield obtained by the same model after disabling the thermal cracking, shown in Fig. 7b, indicates a clear discrepancy in terms of the liquid and

non-condensable gas yields. It is shown that the gas yield remains almost constant and the liquid increases as the temperature increases. This is certainly against the reported experimental observations and the general understanding of the impact of temperature on pyrolysis yield. This result indicates the importance of tar thermal cracking, especially at high temperatures. This also demonstrates the model capabilities in correctly capturing the pyrolysis behavior at increasing temperature.

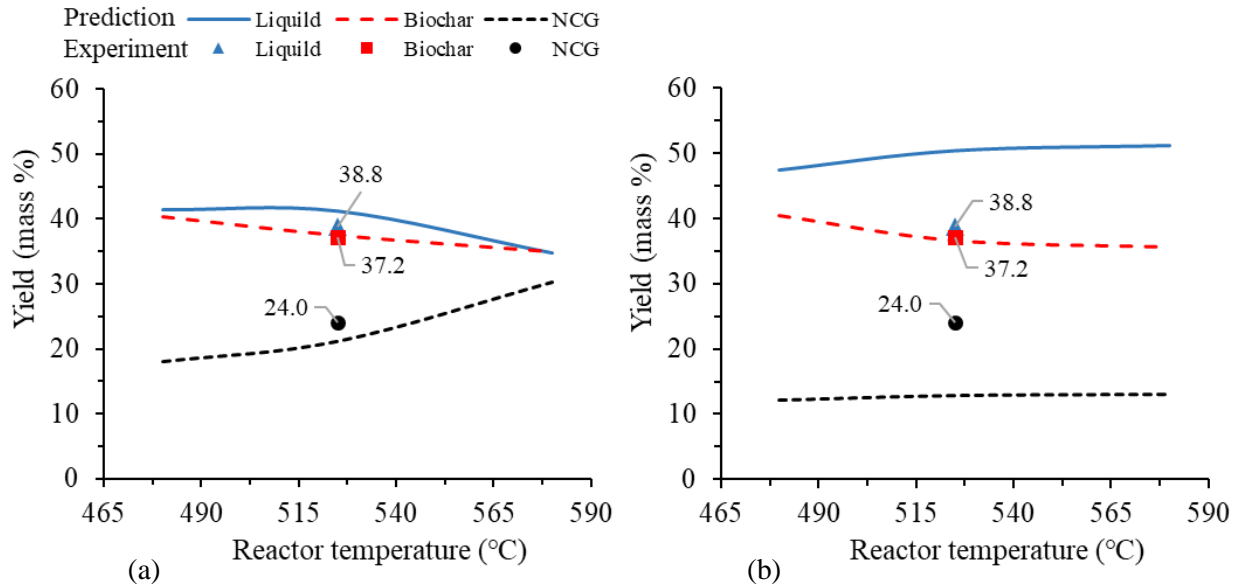


Fig. 7. Predicted pyrolysis yield as function of the pyrolysis temperature in comparison to the experiment result at 525 °C [2] (a) with tar thermal cracking (b) without tar thermal cracking.

3.2.2 Liquid fractions (bio-oil and water)

As mentioned earlier, the pyrolysis liquid is composed of two fractions: a condensable organic phase known as bio-oil, and water derived from the pyrolysis reaction and biomass drying. In Fig. 8, it is observed that the predicted yield of these two components vary with the pyrolysis temperature. At a pyrolysis temperature of 525 °C, the predicted results closely match the experimental findings. The bio-oil yield exhibits a nearly linear decrease from 26.3% to 19.4% as the temperature rises from 480 °C to 580 °C. Conversely, within the same temperature range, the water yield is only increased by 7.6%. The bio-oil decrease is attributed to the thermal cracking of the primary tar₁, leading to the generation of more NCG, as demonstrated earlier in Fig. 7a.

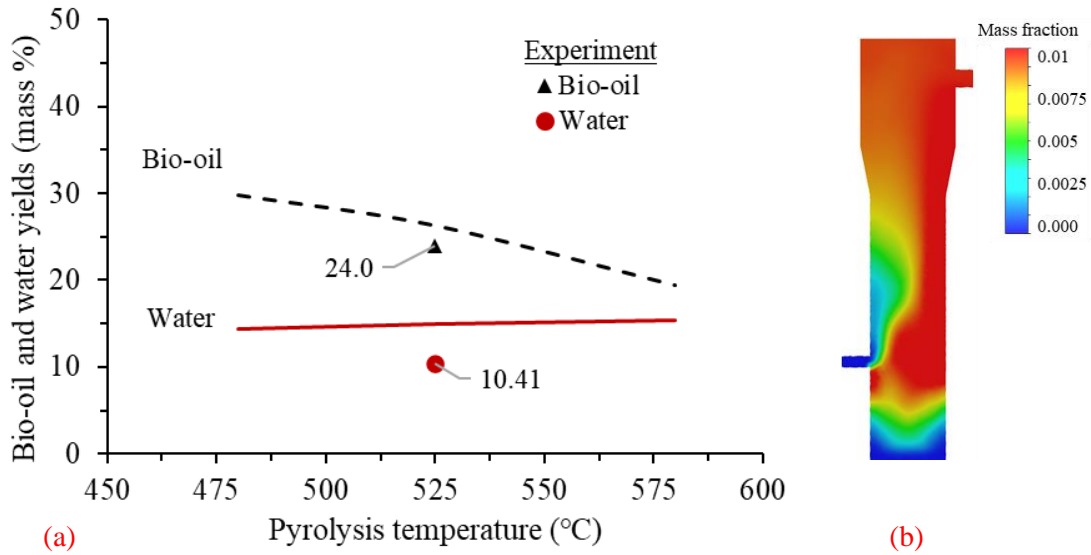


Fig. 8. (a) Bio-oil and water yield as function of the pyrolysis temperature. The symbols represent the experiment results at the temperature of 525 °C [2] (b) Contour of the predicted instantaneous mass fraction of water in the pyrolysis vapor at the temperature of 525 °C. The color code is restricted to 0.01 for better visualization (maximum is 0.03).

3.2.3 Gas velocity and residence time

One of the most important features of fast pyrolysis is the short gas residence time within the hot zone of the reactor. In a fluidized bed reactor, the biomass particles, gases, and bed material all exchange heat at a high rate to release the biomass volatiles (pyrolysis vapor). To enhance the yield of the condensable fraction of the pyrolysis vapor (bio-oil) and minimize thermal cracking, it is crucial to restrict the gas residence time and its interaction with the biochar [4, 5, 35]. The predicted residence time distribution and gas velocities at various pyrolysis temperatures are shown in Fig. 9. The time and spatial averaged axial interstitial gas velocity profiles, shown in Fig. 9a, show an abrupt change in velocity around the region of biomass feeding due to its entrance effect. There are no significant differences in the velocity as the pyrolysis temperature changes from 480 to 580 °C. However, further analysis of the velocity in terms of vector magnitude and

gas residence time distribution reveal noticeable differences, as shown in Figs 9b and 9c, respectively. It is observed that the gas residence time distribution at 525 °C and 580 °C are wider and the corresponding peak residence times are $\tau_p = 0.45$ s and $\tau_p = 0.48$ seconds, compared to shorter time $\tau_p = 0.38$ seconds at 480 °C. While, this is against the ideal gas law, i.e., $v_g \propto \sqrt{T}$, the behavior observed here is believed to be related to the increased turbulence and gas recirculation at high temperatures, as evidently demonstrated by the velocity vectors in Fig. 9b. These results indicate that the pyrolysis temperature, not only affecting the pyrolysis yield, but also affecting the gas residence time distribution and other aspects of the fluidized bed hydrodynamics, as further demonstrated below.

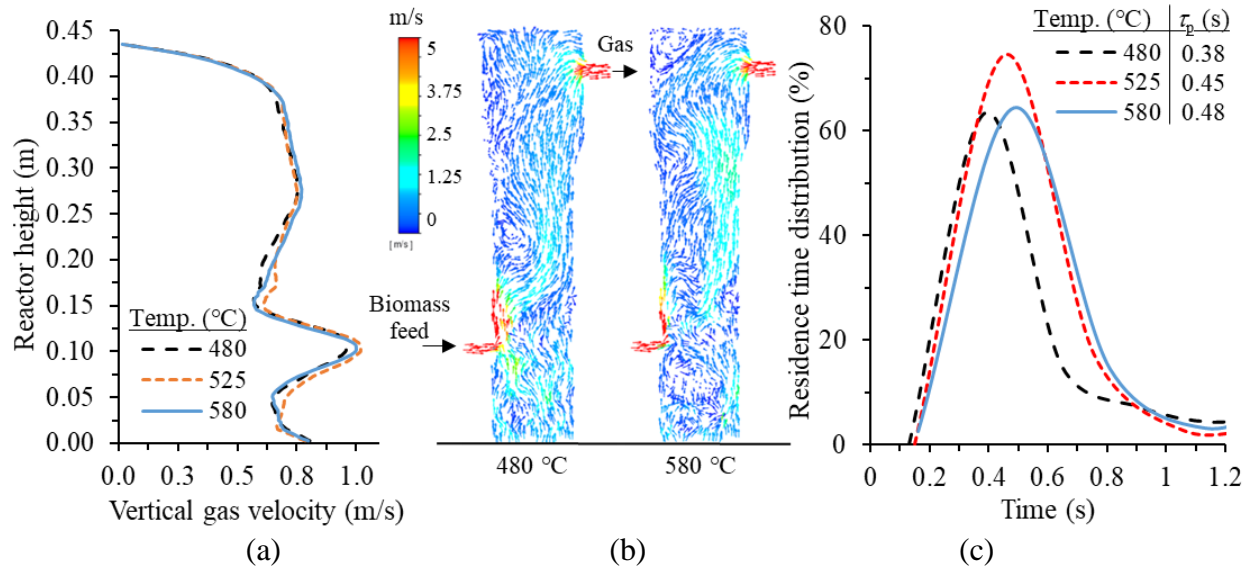


Fig. 9. Pyrolysis gas velocity and residence time at various pyrolysis temperatures (a) cross-sectional average interstitial axial gas velocity profiles (b) vectors of the gas velocity magnitude (c) gas residence time distribution (inset shows the values of the peak residence time at different temperatures).

3.2.4 Solid volume fractions

The spatial variations of the sand volume fraction (concentration) at various pyrolysis temperatures are shown in Fig. 10. The results of the vertical distribution profiles and contours, shown in Fig. 10a and 10b, respectively, indicate a bed expansion up to around two times the initial (static) bed

height, however, no significant variations in the bed expansion as the temperature changes. The formation of bubbles throughout the core of the fluidized bed is well demonstrated in the instantaneous contour in Fig. 10b and the time-averaged radial profiles in Fig. 10c. These are classic features of a bubbling fluidized bed where the bubbles mainly propagate through the core while the wall is covered by a dense solid layer. This layer is estimated here to occupy around 25% of the bed diameter. The radial concentration profiles in Fig. 10c also indicates an increased bubble activities in the core of the bed as the temperature increases and this is well pronounced at 580 °C.

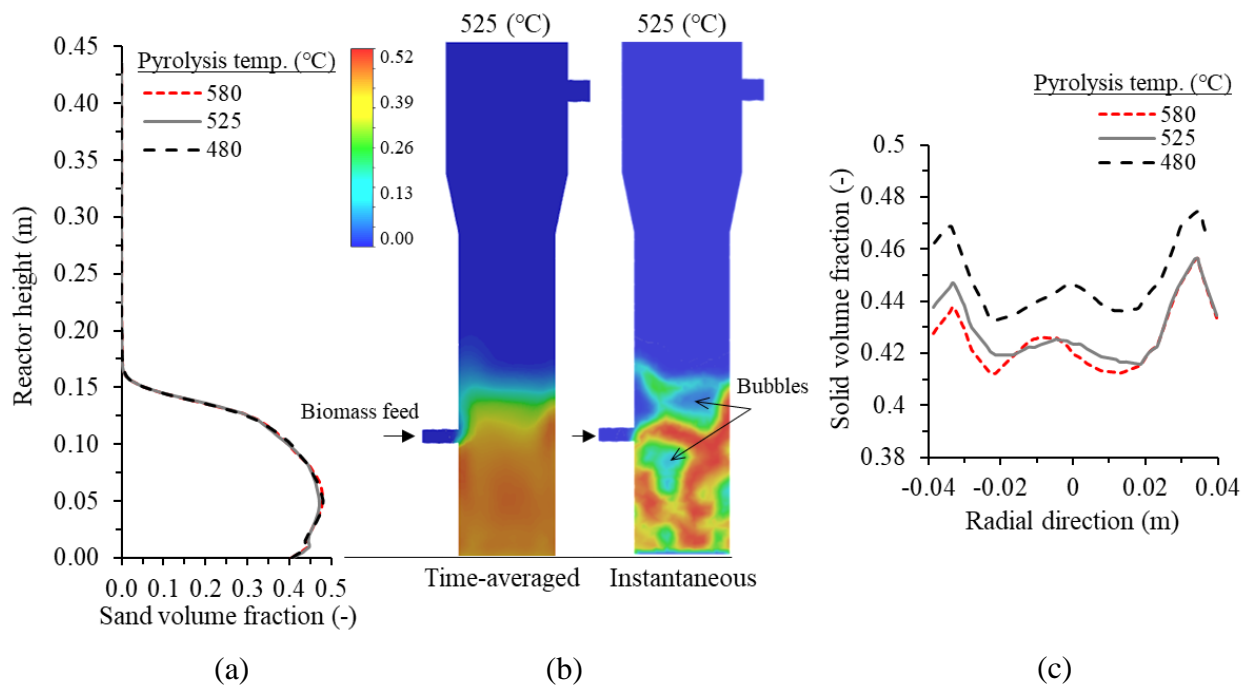


Fig. 10. (a) Time-averaged axial profiles of the sand concentration at various pyrolysis temperatures (b) instantaneous contour of sand concentration at the pyrolysis temperature of 525 °C and (c) time-averaged radial profiles of sand concentration at various pyrolysis temperatures.

The time-averaged axial profiles of the biomass/biochar concentration at the center of the fluidized bed have been found to be more sensitive to the variation of the pyrolysis temperature than the sand, as shown in Fig. 11a. The concentration in the core of the bed becomes more uniform as the temperature increases, as demonstrated in Fig. 11b. The biomass/biochar bed expansion at various temperatures remains around twice the fixed bed height (Figs. 11a and 11b), same as that of the

sand bed but significantly lower in concentration. In a bubbling pyrolysis reactor, limited bed expansion is desirable to ensure quick disengagement of the pyrolysis vapor from the dense biochar and sand bed. This, in turn, reduces the interaction between the solid phases (biochar and sand) and the pyrolysis vapor, thus, reducing the negative impact of thermal and catalytic biochar cracking on the bio-oil yield. The instantaneous contours of the biomass concentration in Fig. 11c shows multiple bubbles at the bottom of the fluidized bed with a large bubble bursting at the top. These are typical features of bubbling fluidized bed commonly reported in the literature [36,37].

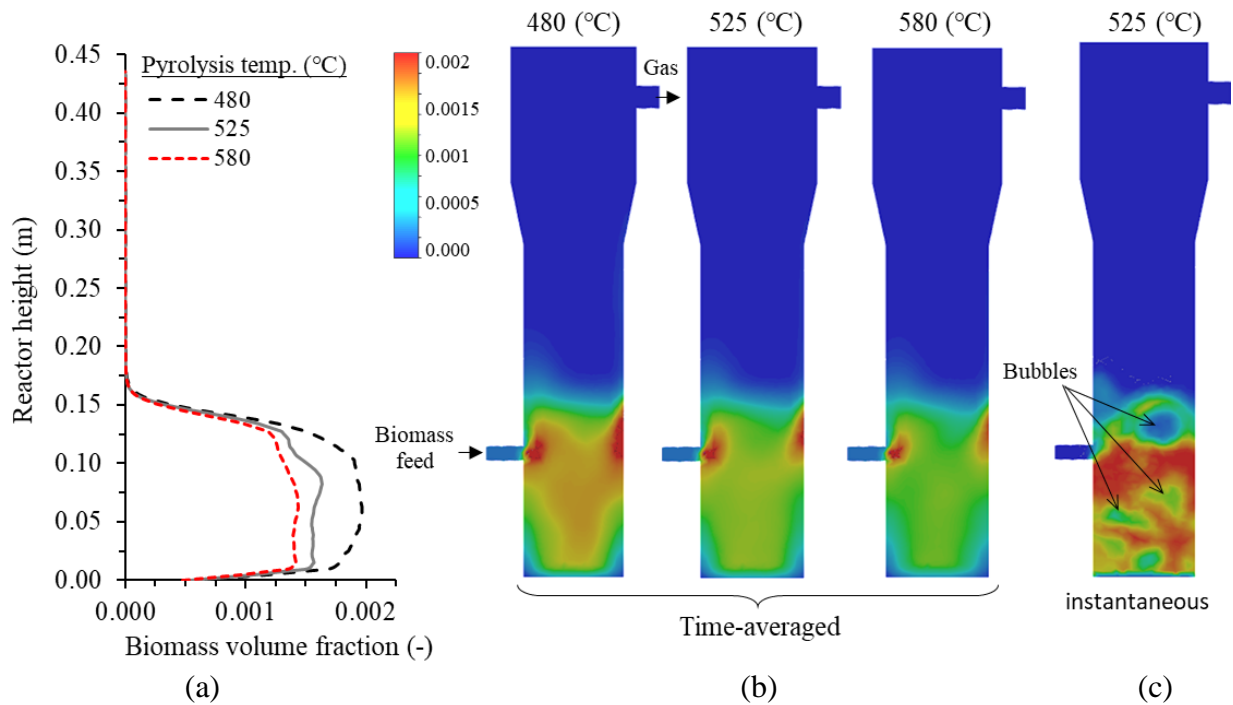


Fig. 11. (a) Time-averaged profiles of biomass concentration at various pyrolysis temperatures (b) time averaged contour of biomass concentration at various pyrolysis temperatures, and (c) instantaneous contours of biomass concentration at the pyrolysis temperature of 525 °C.

3.2.5 Temperature distribution

In fluidized bed pyrolysis, the temperature distribution within the reactor plays a crucial role in defining the pyrolysis yield and product distribution because the pyrolysis reactions are highly temperature dependent. By achieving a uniform temperature, the reaction rate can be consistent throughout the fluidized bed, ensuring that the pyrolysis process proceeds at the desired rate across

the entire reactor volume. The contours in Fig. 12a show that the gas temperature is uniformly distributed throughout the pyrolysis reaction zone. However, the radial temperature profiles in Fig. 12b show a higher temperature near the wall compared to the center, though, this is limited to a maximum of around 5 °C difference. This temperature gradient is primarily attributed to the external heating source applied to the reactor wall. The contours also show that the gas introduced at the biomass feeding at 25 °C, which is meant to create a positive pressure at this region, is shown to be rapidly heated as soon as it enters the fluidized bed, hence, its thermal entrance length is significantly short.

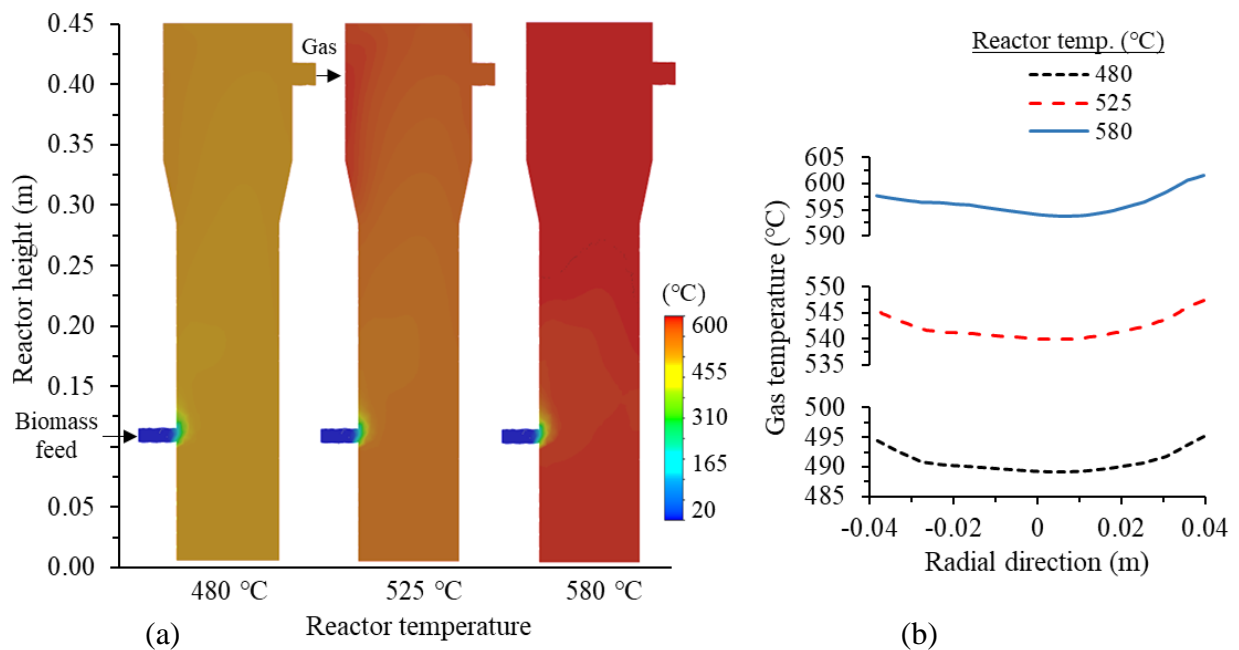


Fig. 12. Gas temperature distribution at different pyrolysis temperatures (a) time-averaged contours (b) time-averaged radial profiles at 0.22 m from the bottom of the reactor.

3.2.6 Devolatilization and thermal tar cracking rates

Fig. 13 illustrates the variation in the devolatilization rate and its efficiency at different pyrolysis temperatures. In Fig. 13a, it is observed that as the temperature increases, the devolatilization rate also increases and becomes more widespread spatially. Additionally, the predictions shown in Fig. 13b demonstrate a nearly positive linear relationship between devolatilization efficiency and

pyrolysis temperature. The predicted devolatilization efficiency at 525°C closely aligns with the experimental measurement, with only a 3.3% overestimation.

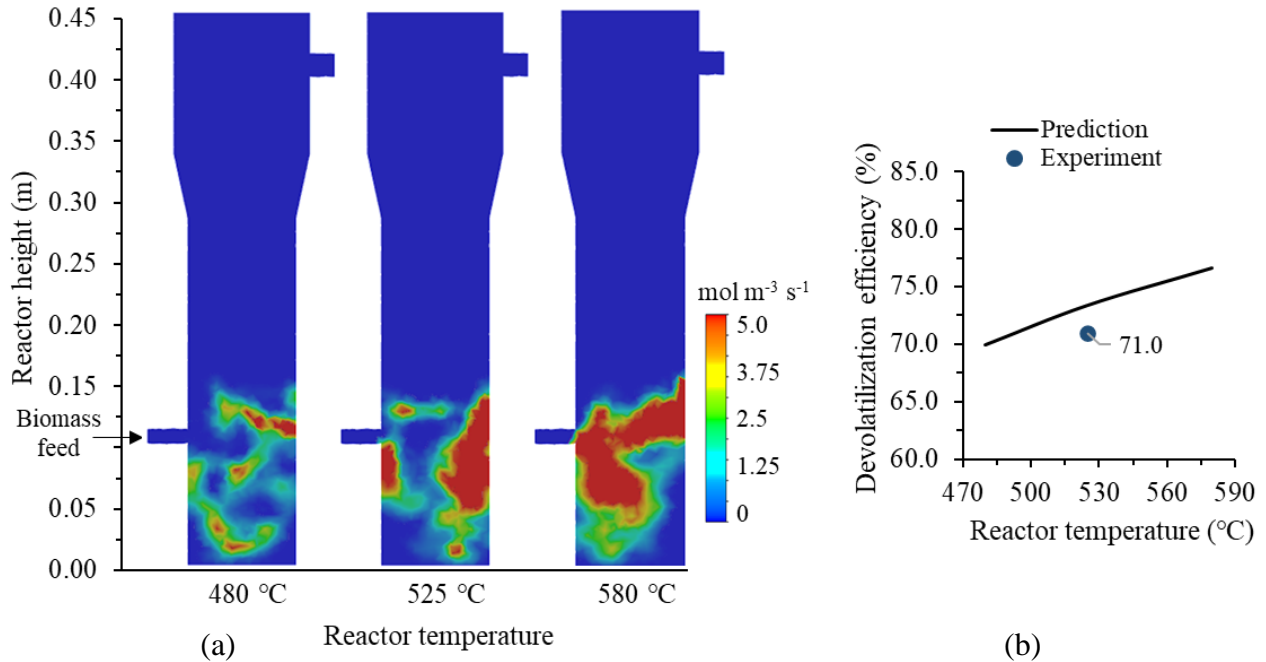


Fig. 13. (a) Contours of instantaneous biomass devolatilization rate at various pyrolysis temperatures, and (b) the corresponding devolatilization efficiency.

The rate of tar thermal cracking at different pyrolysis temperatures is depicted in Fig. 14. It is demonstrated that the cracking process extends spatially and across both the bubbling bed region and the freeboard. At the lower temperature of 480 °C, there is minimal tar thermal cracking. However, as the temperature rises, the cracking rate becomes more significant. At a high temperature of 580°C, the cracking of tar is observed from the bubbling bed region all the way up to the upper part of the freeboard, where there is no contact with the bed material. When thermal cracking takes place, the organic compounds in the pyrolysis vapor decompose, resulting in the production of gases instead of contributing to the bio-oil yield, as previously discussed. This demonstrates the significant influence of tar cracking on the bio-oil yield as the temperature increases. The alignment of these results further strengthens the reliability of the prediction model

and underscores the significance of considering the relationship between tar cracking, temperature, and bio-oil yield when modeling biomass pyrolysis, particularly at temperatures above 500 °C.

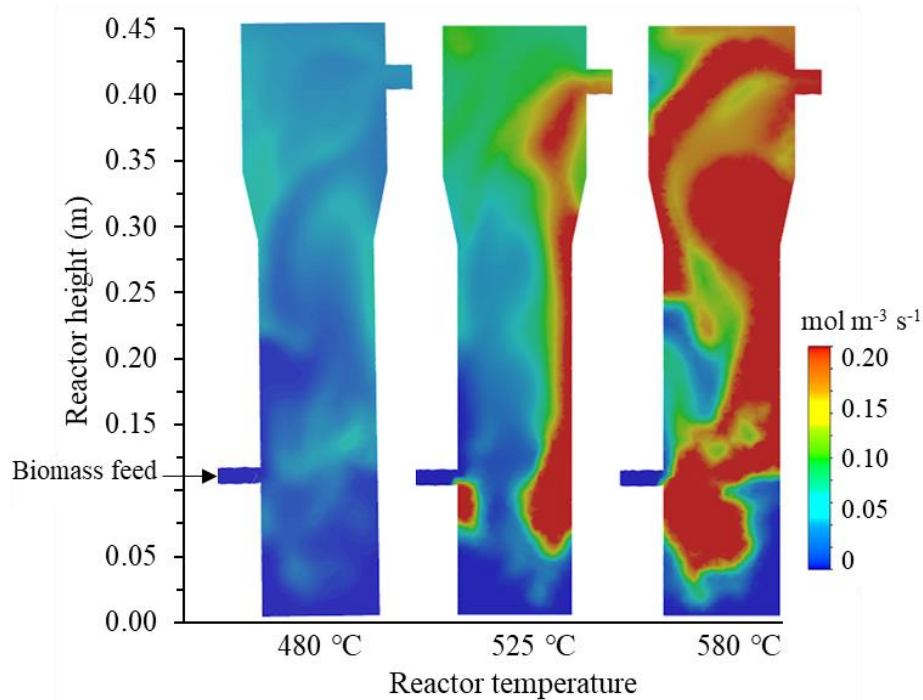


Fig. 14. Contours of the instantaneous thermal tar cracking rate at various pyrolysis temperatures. The color code is restricted to $0.2 \text{ mol m}^{-3} \text{ s}^{-1}$ for better visualization. The predicted maximum devolatilization rate was $2.0 \text{ mol m}^{-3} \text{ s}^{-1}$ at $580 \text{ }^\circ\text{C}$.

4 Remarks on the modeling approach and limitations

Biomass pyrolysis in fluidized bed reactors is a highly complex process that involves multiphase flow, rapid heat transfer and multiple reactions. The model developed in this study has been based on several simplifications to allow simulation at a reasonable computational time while maintaining reasonable accuracy. The adopted Eulerian-Eulerian method, which uses the KTGF for the phase's interactions, comes with its own simplifications, and these are not discussed here. The remarks below briefly touch the hydrodynamics and an extended discussion on the heat transfer and reaction models used.

4.1 Hydrodynamics and heat transfer

- Biomass (date palm waste) is assumed to be a mono-sized mixture of spherically shaped particles. It is recognized that this simplifies a more complex situation, where most waste biomass feedstocks are likely to be in a range of size distribution and irregular in shape. An alternative solution is by introducing multiples sized biomass mixture with a defined sphericity factor; however, this entails a significant increase in the computational time, especially when considering a chemically reactive system. The model also ignores the biomass/biochar shrinkage and breakage at collisions. In the context of this study, these assumptions are reasonable approximations as they may impose limited effect on the accuracy hydrodynamics, e.g., by underestimation of the fluidized bed expansion, bubble size, or biomass heating, but this not expected to impact the accuracy of the pyrolysis predictions critically. Regarding heat transfer, when the particle *Biot* number is below 1.0, the assumption of negligible particle size change is generally considered valid because the particle thermal resistance becomes insignificant. This assumption holds true for the current study.

4.2 Reaction and kinetics

- The derivation of the devolatilization reaction rate and stoichiometric coefficient, as applied in this study, requires a priori knowledge of the relationship between the feedstock biomass and the resulting products. In the context of this study, this refers to the composition of the date palm waste feedstock, and its product bio-oil and biochar. These compositions are typically obtained experimentally through analytical techniques (ultimate and proximate analysis). Therefore, generalization of the developed model requires updated reaction rate kinetics and stoichiometric coefficient if it is to be applied for other biomass feedstocks.
- In the parametrical analysis Section 4.2, assuming that the chemical composition and yield of the pyrolysis products are independent of the pyrolysis temperature, is a simplification of a more complex situation. The yields of these products and their chemical composition may vary, and so the coefficient used in the reactions model (Eq. 11). Nevertheless, this is not expected to cause a significant deviation in the overall model predictions for the range of temperature considered in this study.

- The applied tar thermal cracking reaction and its kinetic (Eqs. 14-16) are generalized ones, i.e., applicable to general woody biomass pyrolysis. Further investigations are required to validate this model for wider biomass types and temperatures.
- There is an argument that part of the pyrolysis vapor may undergo further homogeneous and heterogeneous reactions during pyrolysis. Some of the reported computational studies on biomass pyrolysis (e.g., [18, 38]) consider not only the primary devolatilization reaction but also the possibility of side reactions occurring during pyrolysis. Side reactions are secondary chemical reactions that can take place alongside the main devolatilization reaction. While it is recognized that side reactions can occur during biomass pyrolysis, their significance varies depending on the temperature range being considered. In some cases, at certain temperature ranges, the rates of these side reactions may be relatively low compared to the dominant devolatilization process. In this study it is assumed that side reactions, apart from the thermal cracking of primary tar₁, are unlikely to be of significant effect at the temperature range considered. To demonstrate the validity of this assumption, the reaction rate constant of the most relevant side reactions along with that of the main devolatilization and tar thermal cracking are plotted against a wide range of temperatures in Fig. 15. Here it is evidently clear that the rates of the devolatilization and thermal cracking reactions, shown in Fig. 15a, are several orders of magnitude higher than other possible homogeneous and heterogeneous side reactions, shown in Fig. 15b. The reaction rate constant formulas used to produce the data in Fig. 15b are provided in Appendix Table A3.

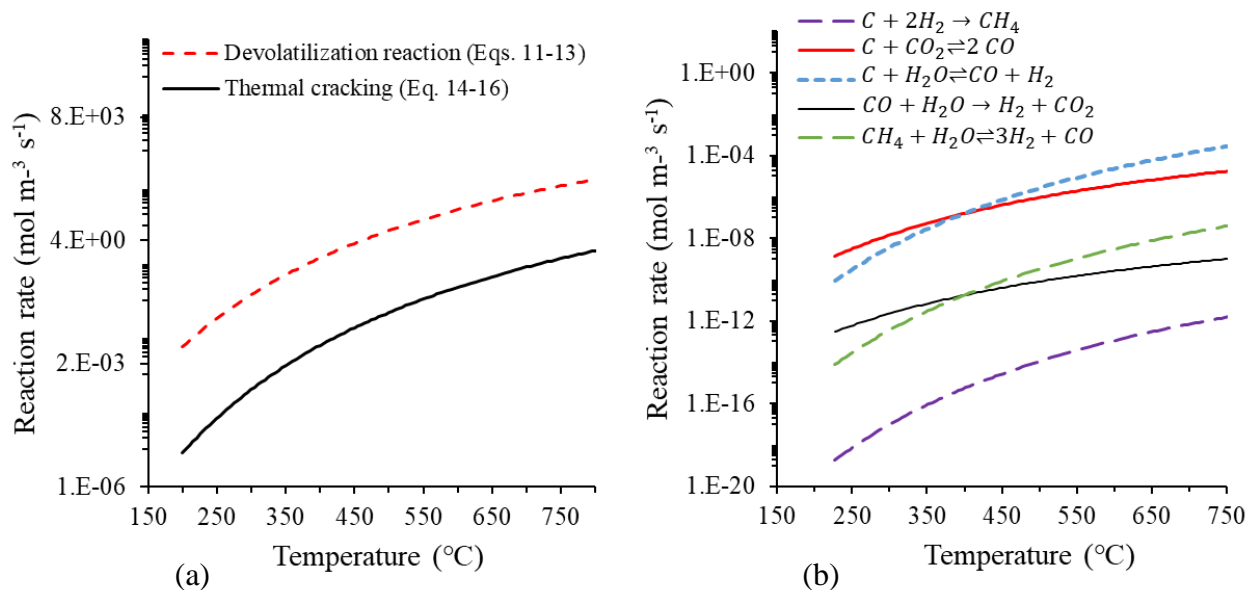


Fig. 15. Calculated reaction rate constants as function of temperature. (a) devolatilization and thermal tar cracking reactions (b) Pyrolysis side reactions.

5 Conclusions

This study introduces a new computational fluid dynamics (CFD) model that simulates the fast pyrolysis of date palm waste in a fluidized bed reactor. Employing the Eulerian-Eulerian approach, the model incorporates a single-step reaction derived from experimental data to depict the devolatilization of date palm waste, along with a secondary tar cracking reaction to capture the entire thermal decomposition and complex hydrocarbons. The accuracy of the model was verified by comparing its predictions to experimental data produced by Makkawi et al. [2]. The main conclusions and remarks on the model validity are as follows:

Model validation (against experimental data of Makkawi et al. [2]):

- The pyrolysis yield of liquid, biochar, and non-condensable gas predicted at the pyrolysis temperature of 525 °C were 41.2%, 37.6% and 21.2% compared to the experimental values of 38.7%, 37.2% and 24%, respectively. The predicted water content in the pyrolysis liquid was 26.3 mass %, whereas the experimental value was 28.3 mass %. The predicted volatile and fixed carbon content of the biochar were 16.6 mass % and 77.9 mass %, compared to

the experimental values of 17.0 mass % and 68.9 mass %, respectively. The predicted fluidized bed temperature was also found to reasonably match the experimental measurement at steady state operation. These findings validate the effectiveness of the developed model in simulating date palm waste fast pyrolysis in a fluidized bed reactor and accurately predicting the quality and quantity of the pyrolysis products.

Parametric analysis (480–580 °C):

- The model correctly predicted classic features of fast pyrolysis at a wide range of temperatures (480-580 °C), where the bio-oil yield drops after reaching a peak, and the non-condensable gas consistently increases with increasing temperature while the biochar decreases. These characteristic features were only obtained after taking into consideration the effect of tar cracking, which become increasingly important as the temperature increases.
- Within the pyrolysis temperatures of 480–580 °C, the liquid yield peaked at 41.5% yield around the pyrolysis temperature of 525 °C, the biochar yield decreased from 40.4% to 36.0%, and the non-condensable gas increased from 18.1% to 30.2%. The yield of pyrolysis water (arising from the biomass drying and devolatilization reaction) was found to increase by around 7% as the temperature increases from 480 °C to 580 °C.
- The analysis of the gas velocity and its distribution across the reactor revealed increased gas recirculation and turbulence with the rise in pyrolysis temperature from 480 °C to 580 °C. This, in turn, led to the widening of the spectrum of gas velocity distribution and an increase in peak velocity. The peak of the gas residence times at the pyrolysis temperatures of 480 °C, 525 °C and 580 °C were 0.38 s, 0.45 s and 0.48 s, respectively, which are well within the recommended range for biomass fast pyrolysis.
- The fluidized bed hydrodynamic analysis indicated limited bed expansion within the temperature range of 480–580 °C, however the contours and radial solid concentration profiles revealed increased bubbles activities within the core of the fluidized bed as the temperature increases.
- The temperature distribution within the fluidized bed and the freeboard were uniform, indicating the absence of any localized hot or cold regions, except the short length at the biomass feeding. This confirms that achieving the desired product quality and selectivity throughout the reactor is a straightforward task within the operating conditions considered.

- The devolatilization efficiency, which is the measure of how effectively volatile compounds are released during pyrolysis, was predicted to be 76.6% at a temperature of 525 °C, compared to the experimental value of 73.7%. The rate of devolatilization rate was also observed to increase in a linear fashion as the temperature increases.
- The model limitations are identified, and the justification of assumptions and simplifications are discussed. In particular, the assumption of negligible side reactions has been validated by quantitative calculation of the rate of reactions and comparing it with the main pyrolysis reactions used.

In conclusion, the developed CFD model demonstrates the potential of an efficient Eulerian-Eulerian computational approach combined with single step reaction for simulating date palm waste pyrolysis within the temperature range of 480-580 °C. This is an essential step contributing to better understanding of a complex thermal process and drive sustainable large-scale solutions in waste management and energy production. However, it is imperative to emphasize the need for further work to address the challenges and limitations discussed in this study.

Declaration of Competing Interest

The authors declare that they have no known competing financial interests or personal relationships that could have appeared to influence the work reported in this paper.

Data availability

Data will be made available on request.

Acknowledgments

The financial supports from the American University of Sharjah is highly acknowledged (FRG19-L-E49). The authors are grateful to Prof. Tony Bridgwater and Dr. Scott Banks (Energy and Bioproducts Research Institute, Birmingham, UK) for their fruitful discussion.

Appendix: Supplementary Material

Table A1. Hydrodynamic model constitutive relations

<p>Gas-solid drag coefficient [39]</p> $\beta_{si} = \frac{3\alpha_{si}\alpha_g\rho_g}{4v_{r,si}^2d_{si}} C_D \left(\frac{Re_{si}}{v_{r,si}} \right) \vec{v}_{si} - \vec{v}_g $ <p>where</p> $C_D = \left(0.63 + \frac{4.8}{\sqrt{Re_{si}/v_{r,si}}} \right)$ $v_{r,si} = 0.5 \left(\alpha_g^{4.14} - 0.06Re_{si} + \sqrt{(0.06Re_{si})^2 + 0.12Re_{si}(\omega - \alpha_g^{4.14}) + \alpha_g^{8.18}} \right)$ <p>where</p> $\omega = 1.6\alpha_s^{1.28} \text{ at } \alpha_g \leq 0.85$ $\omega = 1.6\alpha_s^{1.28} \text{ at } \alpha_g > 0.85$
<p>Solid-solid drag coefficient [39]</p> $K_{ij} = \frac{3(1 + e_{ij}) \left(\frac{\pi}{2} + \frac{\pi^2}{8} C_{f,ij} \right) \rho_{si}\rho_{sj}\varepsilon_{si}\varepsilon_{sj}(d_{si}+d_{sj})^2 g_{0,ij}}{2\pi(\rho_{si}d_{si}^3 + \rho_{sj}d_{sj}^3)} (\vec{v}_{si} - \vec{v}_{sj})$
<p>Solid shear stress [24]</p> $\bar{\tau}_{si} = 2\mu_{si}S$
<p>Granular Viscosity [24,39]</p> $\mu_{si} = \mu_{si,col} + \mu_{si,kin} + \mu_{si,fri}$ $\mu_{si,col} = \frac{4}{5} \varepsilon_{si} d_{si} \rho_{si} g_{0i} (1 + e_{si}) \left(\frac{\theta_{si}}{\pi} \right)^{1/2}$ $\mu_{si,kin} = \frac{\varepsilon_{si} d_{si} \rho_{si} \sqrt{\theta_{si} \pi}}{6(1-\varepsilon_{si})} \left[1 + \frac{2}{5} (1 + e_{si}) (3e_{si} - 1) \varepsilon_{si} g_{0i} \right]$ $\mu_{si,fr} = \frac{p_{si} \sin \phi}{2\sqrt{I_{2D}}}$
<p>Solids pressure [39]</p>

$P_{si} = \alpha_{si}\rho_{si}\theta_{si} + 2\alpha_{si}\rho_{si}\theta_{si} \sum_{j=1}^2 \left[\frac{(d_{si} + d_{sj})}{2d_{si}} \right]^3 (1 + e_{s,ij})g_{0,ij}\alpha_{s,ij}$
<p>Radial distribution function [39]</p> $g_{0,ij} = \frac{g_{0i}d_{si} + g_{0j}d_{sj}}{d_{si} + d_{sj}}$ $g_{0i} = \left[1 - \left(\frac{\alpha_{s,all}}{\alpha_{s,max}} \right)^{1/3} \right]^{-1} + \frac{1}{2} d_{si} \sum_{j=1}^2 \frac{\alpha_{sj}}{d_{sj}}$ <p>where $\varepsilon_{s,all} = \sum_j^2 \varepsilon_{sj}$</p>
<p>Energy dissipation [24,39,40]</p> $\gamma_{\theta_{si}} = \frac{12(1 - e_{ss}^2)}{d_s \pi^2} \alpha_s^2 \rho_s \theta_{si}^{\frac{3}{2}}$
<p>Energy diffusion coefficient [39]</p> $\kappa_{\theta_{si}} = \frac{150\rho_{si}d_{si}(\pi\theta_{si})^{\frac{1}{2}}}{384(e_{ss} + 1)g_{0,si}} \left[1 + \frac{6}{5} \alpha_{si}g_{0,si}(e_{ss} + 1) \right]^2 + 2\alpha_{si}^2\rho_{si}d_{si}g_{0,si}(e_{ss} + 1) \left(\frac{\theta_{si}}{\pi} \right)^{\frac{1}{2}}$
<p>Kinetic energy exchange between solid and fluid [24,40]</p> $\varphi_{l_{si}} = -3K_{isl}\theta$ $K_{sil} = \frac{3C_d Re_s}{4v_{r,si}^2 d_s^2} \alpha_{si}\alpha_l$

* i or $j = 1$ or 2 ($i \neq j$) refers to the solid phases in the fluidized bed (biomass and sand)

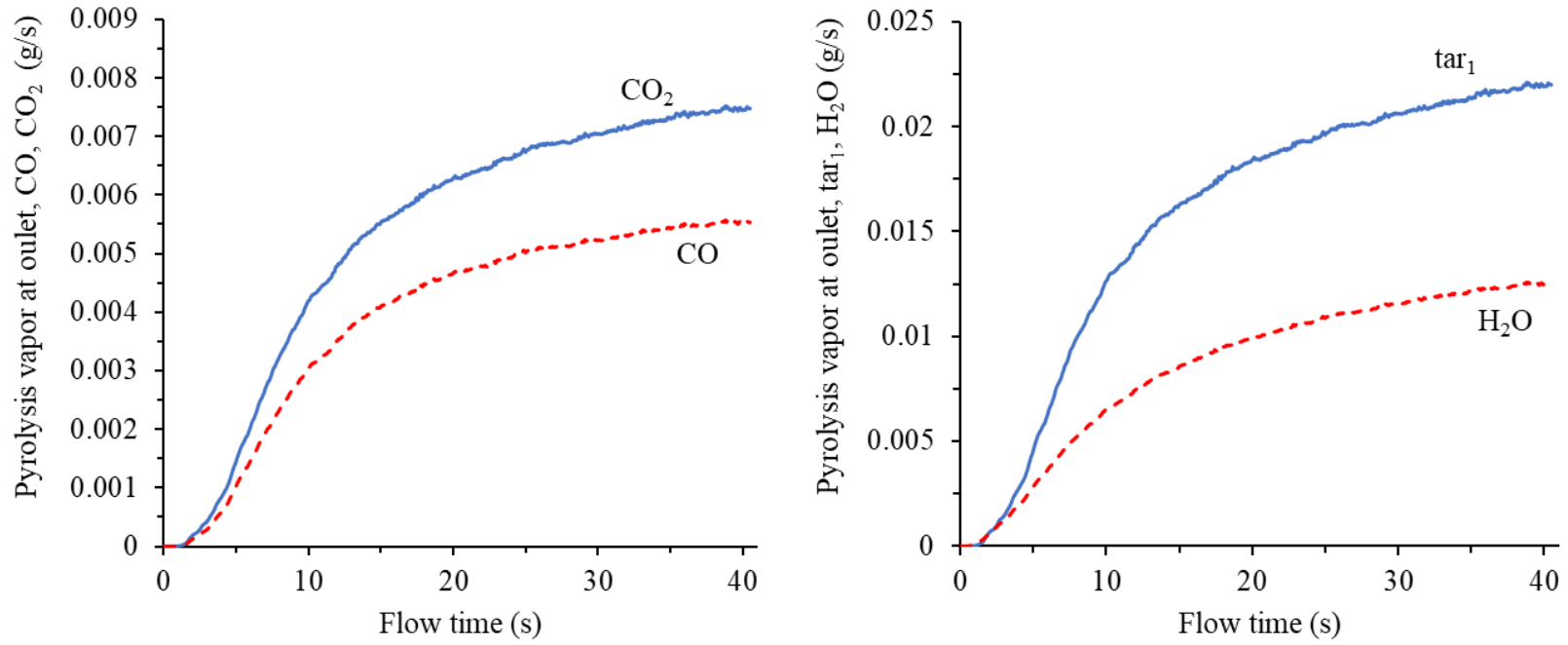
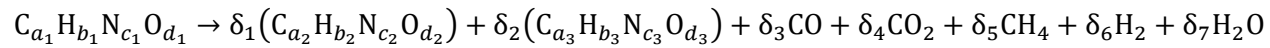


Fig. A1: Evolution of selected pyrolysis vapor component produced at the pyrolysis temperature of 525 °C.

Table A2: Equations used in the calculation of pyrolysis reaction coefficient.



Atomic balance	
Carbon balance	$a_2\delta_1 + a_3\delta_2 + \delta_3 + \delta_4 + \delta_5 = a_1$
Hydrogen balance	$b_2\delta_1 + b_3\delta_2 + 4\delta_5 + 2\delta_6 + 2\delta_7 = b_1$
Oxygen balance	$d_2\delta_1 + d_3\delta_2 + \delta_3 + 2\delta_4 + \delta_7 = d_1$
Mass balance	

Carbon monoxide	$\frac{\%CO}{\%CO_2} = \frac{MW_{CO}\delta_3}{MW_{CO_2}\delta_4}$
Methane	$\frac{\%CH_4}{\%CO_2} = \frac{MW_{CH_4}\delta_5}{MW_{CO_2}\delta_4}$
Hydrogen	$\frac{\%H_2}{\%CO_2} = \frac{MW_{H_2}\delta_6}{MW_{CO_2}\delta_4}$
Overall	$MW_{tar_1}\delta_1 + MW_{biochar}\delta_2 + MW_{CO}\delta_3 + MW_{CO_2}\delta_4 + MW_{CH_4}\delta_5 + MW_{H_2}\delta_6 + MW_{H_2O}\delta_7 = MW_{biomass}$

Table A3. Reactions rate and kinetics of the heterogeneous and homogeneous reactions to produce the data in Fig. 15.

Heterogeneous Reactions		
Hydrogasification [25] $C + 2H_2 \rightarrow CH_4$	$r = k[C_{H_2}]$	$A = 3.42 \times 10^{-3} \text{ s}^{-1}$ $E = 1.29 \times 10^5 \text{ J mol}^{-1}$
Boudouard [25] $C + CO_2 \rightleftharpoons 2CO$	$r = k[C_{CO_2}]$	$A = 36.2 \text{ s}^{-1}$ $E = 7.7 \times 10^4 \text{ J mol}^{-1}$
Water-Gas [25] $C + H_2O \rightleftharpoons CO + H_2$	$r = k[C_{H_2O}]$	$A = 1.52 \times 10^4 \text{ s}^{-1}$ $E = 1.22 \times 10^5 \text{ J kmol}^{-1}$
Homogeneous Reactions		
Water-gas shift [25] $CO + H_2O \rightarrow H_2 + CO_2$	$r = k[C_{CO}][C_{H_2O}]$	$A = 0.0265 \text{ s}^{-1}$ $E = 6.6 \times 10^4 \text{ J kmol}^{-1}$
Steam Methane Reforming [41] $CH_4 + H_2O \rightleftharpoons 3H_2 + CO$	$r = k[C_{CH_4}][C_{H_2O}]$	$A = 3.02 \times 10^3$ $E = 1.25 \times 10^5 \text{ J kmol}^{-1}$

Nomenclature

C_d	particle drag coefficient (-)
C_{fr}	friction coefficient (-)
d_s	solids diameter (m)
e_{ss}	coefficient of restitution for particle collisions (=0.9) (-)
g_0	radial distribution function (-)
\vec{g}	gravity ($m\ s^{-2}$)
I_{2D}	second invariant of the deviatoric stress tensor (-)
\bar{I}	unit tensor (-)
K	solid-solid momentum exchange coefficient ($kg\ m^{-3}\ s^{-1}$)
k_{θ_s}	Kinetic diffusion coefficient ($kg\ m^{-3}\ s^{-1}$)
k_s	The thermal conductivity coefficient ($W\ m^{-1}\ K$)
Nu_s	Nusselt number (-)
P	pressure (Pa)
Q_{gsi}	Heat transfer coefficient ($W\ m^{-2}\ K^{-1}$)
S	strain rate tensor (s^{-1})
S_q	Source term in momentum equation ($kg\ m^3\ s^{-1}$)
t	Time (s)
v	Solids velocity vector ($m\ s^{-1}$)

Greek letters

β	momentum exchange coefficient ($kg\ m^{-3}\ s^{-1}$)
μ	viscosity ($kg\ m^{-1}\ s^{-1}$)
ρ	Density ($kg\ m^{-3}$)
α	phase volume fraction (-)
θ_s	granular temperature ($m\ s^{-2}$)
$\bar{\tau}_s$	stress tensor (Pa)
γ_{θ_s}	collisional dissipation of energy ($kg\ m^{-1}\ s^{-3}$)
φ_{ls}	energy exchange between the fluid and solid ($kg\ m^{-1}\ s^{-3}$)
Φ	angle of internal friction (-)
δ, γ	reaction equations stoichiometry coefficients (-)

Subscript

s, g	solid and gas phases, respectively
l	fluid
col	collision
kin	kinetic
fri	friction

References

- [1] D. Czajczyńska, L. Anguilano, H. Ghazal, R. Krzyżyńska, A. J. Reynolds, N. Spencer, and H. Jouhara, “Potential of pyrolysis processes in the waste management sector,” *Therm. Sci. Eng. Prog.*, vol. 3, pp. 171–197, Sep. 2017, doi: 10.1016/j.tsep.2017.06.003.
- [2] Y. Makkawi, Y. El Sayed, M. Salih, P. Nancarrow, S. Banks, and T. Bridgwater, “Fast pyrolysis of date palm (*Phoenix dactylifera*) waste in a bubbling fluidized bed reactor,” *Renew. Energy*, vol. 143, pp. 719–730, Dec. 2019, doi: 10.1016/j.renene.2019.05.028.
- [3] Y. El may, M. Jeguirim, S. Dorge, G. Trouvé, and R. Said, “Study on the thermal behavior of different date palm residues: Characterization and devolatilization kinetics under inert and oxidative atmospheres,” *Energy*, vol. 44, no. 1, pp. 702–709, Aug. 2012, doi: 10.1016/j.energy.2012.05.022.
- [4] S. R. A. Kersten, X. Wang, W. Prins, and W. P. M. van Swaaij, “Biomass Pyrolysis in a Fluidized Bed Reactor. Part 1: Literature Review and Model Simulations,” *Ind. Eng. Chem. Res.*, vol. 44, no. 23, pp. 8773–8785, Nov. 2005, doi: 10.1021/ie0504856.
- [5] A. V. Bridgwater, D. Meier, and D. Radlein, “An overview of fast pyrolysis of biomass,” *Org. Geochem.*, vol. 30, no. 12, pp. 1479–1493, Dec. 1999, doi: 10.1016/S0146-6380(99)00120-5.
- [6] M. Iguchi and O. Ilegbusi, “Modeling Multiphase Materials Processes: Gas-Liquid Systems. Springer, New York,” 2011.
- [7] J. W. Chew, W. C. Q. LaMarche, and R. A. Cocco, “100 years of scaling up fluidized bed and circulating fluidized bed reactors,” *Powder Technol.*, vol. 409, p. 117813, Sep. 2022, doi: 10.1016/j.powtec.2022.117813.
- [8] X. Li, C. Yin, S. Knudsen Kær, and T. Condra, “A detailed pyrolysis model for a thermally large biomass particle,” *Fuel*, vol. 278, p. 118397, Oct. 2020, doi: 10.1016/j.fuel.2020.118397.
- [9] H. Uwitonze, A. Kim, H. Kim, B. Brigljević, H. Vu Ly, S.-S. Kim, M. Upadhyay, and H. Lim, “CFD simulation of hydrodynamics and heat transfer characteristics in gas–solid circulating fluidized bed riser under fast pyrolysis flow condition,” *Appl. Therm. Eng.*, vol. 212, p. 118555, Jul. 2022, doi: 10.1016/j.applthermaleng.2022.118555.
- [10] F. A. Elewuwa and Y. T. Makkawi, “Hydrogen production by steam reforming of DME in a large scale CFB reactor. Part I: Computational model and predictions,” *Int. J. Hydrogen Energy*, vol. 40, no. 46, pp. 15865–15876, Dec. 2015, doi: 10.1016/j.ijhydene.2015.10.050.
- [11] T. Chen, X. Ku, J. Lin, and H. Ström, “CFD-DEM Simulation of Biomass Pyrolysis in Fluidized-Bed Reactor with a Multistep Kinetic Scheme,” *Energies*, vol. 13, no. 20, p. 5358, Oct. 2020, doi: 10.3390/en13205358.
- [12] M. Baniasadi, M. Baniasadi, and B. Peters, “Coupled CFD-DEM with heat and mass transfer to investigate the melting of a granular packed bed,” *Chem. Eng. Sci.*, vol. 178,

- pp. 136–145, Mar. 2018, doi: 10.1016/j.ces.2017.12.044.
- [13] Z. Zou, Y. Ge, J. Zhu, J. Wang, Q. Zhu, and H. Li, “Industrial practice and CFD investigation of a multi-chamber fluidized bed reactor for MnO₂ ore reduction,” *Chem. Eng. J.*, vol. 455, p. 140732, Jan. 2023, doi: 10.1016/j.cej.2022.140732.
- [14] H. Sun, S. Yang, G. Bao, K. Luo, J. Hu, and H. Wang, “CFD investigation of the complex multiphase flow of biomass gasification in industrial-scale dual fluidized bed reactor,” *Chem. Eng. J.*, vol. 457, p. 141312, Feb. 2023, doi: 10.1016/j.cej.2023.141312.
- [15] M. Bashir, X. Yu, M. Hassan, and Y. Makkawi, “Modeling and Performance Analysis of Biomass Fast Pyrolysis in a Solar-Thermal Reactor,” *ACS Sustain. Chem. Eng.*, vol. 5, no. 5, pp. 3795–3807, May 2017, doi: 10.1021/acssuschemeng.6b02806.
- [16] D. Tokmurzin, J. Y. Nam, S. J. Park, S. J. Yoon, T.-Y. Mun, S. M. Yoon, J. H. Moon, J. G. Lee, D. H. Lee, H. W. Ra, and M. W. Seo, “Three-Dimensional CFD simulation of waste plastic (SRF) gasification in a bubbling fluidized bed with detailed kinetic chemical model,” *Energy Convers. Manag.*, vol. 267, p. 115925, Sep. 2022, doi: 10.1016/j.enconman.2022.115925.
- [17] L. von Berg, A. Anca-Couce, C. Hochenauer, and R. Scharler, “Multi-scale modelling of a fluidized bed biomass gasifier of industrial size (1 MW) using a detailed particle model coupled to CFD: Proof of feasibility and advantages over simplified approaches,” *Energy Convers. Manag.*, vol. 286, p. 117070, Jun. 2023, doi: 10.1016/j.enconman.2023.117070.
- [18] R. Houston, O. Oyediji, and N. Abdoulmoumine, “Detailed biomass fast pyrolysis kinetics integrated to computational fluid dynamic (CFD) and discrete element modeling framework: Predicting product yields at the bench-scale,” *Chem. Eng. J.*, vol. 444, p. 136419, Sep. 2022, doi: 10.1016/j.cej.2022.136419.
- [19] S. Jalalifar, R. Abbassi, V. Garaniya, K. Hawboldt, and M. Ghiji, “Parametric analysis of pyrolysis process on the product yields in a bubbling fluidized bed reactor,” *Fuel*, vol. 234, pp. 616–625, Dec. 2018, doi: 10.1016/j.fuel.2018.07.070.
- [20] S. Hameed, A. Sharma, and V. Pareek, “A distributed activation energy model for cellulose pyrolysis in a fluidized bed reactor,” *Chem. Eng. Res. Des.*, vol. 191, pp. 414–425, Mar. 2023, doi: 10.1016/j.cherd.2023.01.048.
- [21] L. Cai, Q. Wang, Q. Xiong, X. Wang, L. Fu, L. Han, Z. Wang, and Y. Zhou, “Numerical simulation and multi-process coupling analysis for biomass pyrolysis fluidized bed reactor based on synergistic effects between biomass and nitrogen inlet modes,” *J. Anal. Appl. Pyrolysis*, vol. 169, p. 105801, Jan. 2023, doi: 10.1016/j.jaap.2022.105801.
- [22] Thoharudin, Y.-S. Chen, and S.-S. Hsiau, “Numerical Studies on Fast Pyrolysis of Palm Kernel Shell in a Fluidized Bed Reactor,” *IOP Conf. Ser. Mater. Sci. Eng.*, vol. 874, no. 1, p. 012033, Jun. 2020, doi: 10.1088/1757-899X/874/1/012033.
- [23] K. Ding, Q. Xiong, Z. Zhong, D. Zhong, and Y. Zhang, “CFD simulation of combustible solid waste pyrolysis in a fluidized bed reactor,” *Powder Technol.*, vol. 362, pp. 177–187, Feb. 2020, doi: 10.1016/j.powtec.2019.12.011.
- [24] A. Fluent, “ANSYS Fluent 2021 R1 user’s guide and theory manual,” *Ansys Fluent Inc*,

2021.

- [25] S. Gerber, F. Behrendt, and M. Oevermann, “An Eulerian modeling approach of wood gasification in a bubbling fluidized bed reactor using char as bed material,” *Fuel*, vol. 89, no. 10, pp. 2903–2917, Oct. 2010, doi: 10.1016/j.fuel.2010.03.034.
- [26] X. Yu, M. Hassan, R. Ocone, and Y. Makkawi, “A CFD study of biomass pyrolysis in a downer reactor equipped with a novel gas–solid separator-II thermochemical performance and products,” *Fuel Process. Technol.*, vol. 133, pp. 51–63, May 2015, doi: 10.1016/j.fuproc.2015.01.002.
- [27] D. J. Gunn, “Transfer of heat or mass to particles in fixed and fluidised beds,” *Int. J. Heat Mass Transf.*, vol. 21, no. 4, pp. 467–476, Apr. 1978, doi: 10.1016/0017-9310(78)90080-7.
- [28] Kissinger HE. Variation of peak temperature with heating rate in differential thermal analysis. *J. Res. Natl. Inst. Stan.* 1956;57:217e21.
- [29] J. P. Diebold, “The cracking kinetics of depolymerized biomass vapors in a continuous, tubular reactor,” Colorado School of Mines, 1985.
- [30] M. Abdullahi, “A novel approach for integrating concentrated solar energy with biomass thermochemical conversion processes,” 2016.
- [31] K. Raveendran and A. Ganesh, “Heating value of biomass and biomass pyrolysis products,” *Fuel*, vol. 75, no. 15, pp. 1715–1720, Nov. 1996, doi: 10.1016/S0016-2361(96)00158-5.
- [32] J. Eke, J. A. Onwudili, and A. V. Bridgwater, “Influence of Moisture Contents on the Fast Pyrolysis of Trommel Fines in a Bubbling Fluidized Bed Reactor,” *Waste and Biomass Valorization*, vol. 11, no. 7, pp. 3711–3722, Jul. 2020, doi: 10.1007/s12649-018-00560-2.
- [33] F. A. Elewuwa and Y. T. Makkawi, “A computational model of hydrogen production by steam reforming of dimethyl ether in a large scale CFB reactor. Part II: Parametric analysis,” *Int. J. Hydrogen Energy*, vol. 41, no. 44, pp. 19819–19828, Nov. 2016, doi: 10.1016/j.ijhydene.2016.08.072.
- [34] Y. Makkawi, M. Khan, F. H. Pour, O. Moussa, B. Mohamed, H. Alnoman, and Y. Elsayed, “A comparative analysis of second-generation biofuels and its potentials for large-scale production in arid and semi-arid regions,” *Fuel*, vol. 343, p. 127893, Jul. 2023, doi: 10.1016/j.fuel.2023.127893.
- [35] A. Bridgwater, “Fast pyrolysis processes for biomass,” *Renew. Sustain. Energy Rev.*, vol. 4, no. 1, pp. 1–73, Mar. 2000, doi: 10.1016/S1364-0321(99)00007-6.
- [36] P. Chobthiangtham, S. Fukuda, and P. Piumsomboon, “Comparison of Hydrodynamic Behavior inside Bed Zone with Non-Simplified and Simplified Air Distributor in a Bubbling Fluidized Bed Gasifier Model,” *J. Sustain. Energy Environ.*, vol. 5, pp. 117–125, 2014.
- [37] Y. . Makkawi and P. . Wright, “Fluidization regimes in a conventional fluidized bed characterized by means of electrical capacitance tomography,” *Chem. Eng. Sci.*, vol. 57,

- no. 13, pp. 2411–2437, Jul. 2002, doi: 10.1016/S0009-2509(02)00138-0.
- [38] S. Q. Sia and W.-C. Wang, “Numerical simulations of fluidized bed fast pyrolysis of biomass through computational fluid dynamics,” *Renew. Energy*, vol. 155, pp. 248–256, Aug. 2020, doi: 10.1016/j.renene.2020.03.134.
- [39] M. I. Hassan and Y. T. Makkawi, “A hydrodynamic model for biomass gasification in a circulating fluidized bed riser,” *Chem. Eng. Process. - Process Intensif.*, vol. 129, pp. 148–161, Jul. 2018, doi: 10.1016/j.cep.2018.05.012.
- [40] D. Gidaspow, *Multiphase flow and fluidization: continuum and kinetic theory descriptions*. Academic press, 1994.
- [41] V. Pasangulapati, *Devolatilization characteristics of cellulose, hemicellulose, lignin and the selected biomass during thermochemical gasification: experiment and modeling studies*. Oklahoma State University, 2012.